# Technical note: A decoupled in situ framework for aerosol multi-wavelength optical properties: application for lidar retrievals

Cheng Yao[1], Longlong Wang[1,*], Aoxiang Huang[1], Bin Zhang[1], Marija Bervida Mačak[2], Luka Drinovec[2], Asta Gregorič[2,3], Fei Gao[4], Janja Vaupotič[5], Miloš Miler[6], Mateja Gosar[6], Zhangwei Yu[1], Daru Chen[1], Griša Močnik[2], Samo Stanič[2]

[1]Hangzhou Institute of Advanced Studies, Zhejiang Normal University, Hangzhou, 311231, China
[2]Center for Atmospheric Research, University of Nova Gorica, Nova Gorica 5270, Slovenia
[3]Aerosol d.o.o., Ljubljana 1000, Slovenia
[4]School of Optoelectronic Science and Intelligent Instrumentation, Xi'an University of Technology, Xi'an, 710048, China
[5]Jožef Stefan Institute, Ljubljana 1000, Slovenia
[6]Geological Survey of Slovenia, Ljubljana 1000, Slovenia

*Correspondence to*: Longlong Wang (longlong.wang@zjnu.edu.cn)

Abstract. Accurate constraints on aerosol complex refractive index (CRI), single scattering albedo (SSA), and lidar ratio (LR) are essential for improving lidar-based aerosol retrievals and reducing radiative-effect uncertainties. However, consistent derivation from in situ observations remains challenging in complex mixed-aerosol environments, where size distribution, absorption, and humidity effects are strongly coupled. Here we present a decoupled inversion framework that integrates SMPS–OPC size distributions, AE33-derived absorption coefficients, and ambient relative humidity observations from the Vipava Valley (Slovenia) in April 2016 to derive dry-state homogeneous-equivalent CRI and RH-corrected lidar-relevant SSA and LR at 355, 532, and 1064 nm. The framework reconstructs a continuous particle size distribution through instrument-response-aware SMPS–OPC geometric alignment and retrieves the reference real refractive index. AE33-derived absorption constraints and a singly subtractive Kramers–Kronig (SSKK) relation are then used to derive the ~~a spectrally consistent~~ dry-state CRI spectrum, after which SSA and LR are recalculated through an RH-corrected wet-state forward optical calculation. The retrieved dry-state mean *n* values were 1.44~~9~~8, 1.441, and 1.~~437~~437, and the mean *k* values were 0.030~~9~~12, 0.023~~5~~8, and 0.019~~0~~2 at 355, 532, and 1064 nm, respectively. The RH-corrected mean SSA values were 0.85~~5~~66, 0.841~~5~~2, and 0.760~~7~~4, and the corresponding mean LR values were 86.5~~3~~4, 5~~7~~8.5~~9~~4, and 39.8~~1~~2 sr. Sensitivity tests showed that the AE33 effective multiple-scattering correction affects absorption-sensitive products, with $C_{\mathrm{eff}} = 5$ selected as a reference scenario for sensitivity reporting.~~used as a site- and period-specific baseline.~~ The framework provides a practical pathway for linking dry in situ CRI retrievals with RH-corrected multi-wavelength lidar-relevant aerosol optical products.

## 1 Introduction

Aerosols profoundly influence the regional and global radiative balance through their interactions with solar and terrestrial radiation (Bond et al., 2013; Chen et al., 2022; Myhre et al., 2013). Therefore, robust constraints on aerosol optical properties relevant to radiative transfer and remote sensing are of critical significance for climate modelling and remote sensing retrievals. Among these properties, the complex refractive index (CRI) links aerosol composition and size distribution to scattering and absorption, SSA characterizes the partitioning between scattering and extinction, and LR, defined as the ratio of the aerosol extinction coefficient to the backscatter coefficient, serves as a crucial parameter in lidar retrievals for reconstructing extinction profiles from backscattered signals. In addition, SSA is a key parameter for evaluating aerosol radiative effects and absorption strength (Elsey et al., 2024), whereas LR is widely used as a diagnostic intensive optical property for aerosol typing and the assumption for elastic lidar inversion (Floutsi et al., 2023). The CRI is also an important input for retrieving aerosol microphysical properties from lidar observations (Müller et al., 2016). Together, these wavelength-dependent optical properties provide complementary constraints on aerosol absorption, size structure, and optical state, and their spectral behaviour contains additional information on aerosol composition and mixing state (Cheng et al., 2024; Haarig et al., 2025).

As lidar remote sensing is widely used to retrieve the vertical distribution of aerosol optical and microphysical properties (Floutsi et al., 2023; Liu et al., 2024), the ultraviolet, visible, and near-infrared wavelengths of 355, 532, and 1064 nm are of particular interest because they correspond to the standard operating wavelengths of multi-wavelength aerosol lidar systems and are widely used for aerosol optical characterization (Haarig et al., 2025; Böckmann et al., 2024). Simultaneous characterization of CRI, SSA, and LR at these wavelengths therefore provides aerosol-state-dependent optical constraints~~prior information for~~ relevant to lidar retrievals. In situ aerosol measurements have previously been used with Mie calculations to derive lidar ratios and compare them with lidar-based products (Eswaran et al., 2023), while ground-based aerosol observations have also been evaluated against Raman-lidar retrievals under suitable boundary-layer conditions (Liu et al., 2024). These studies illustrate how locally constrained aerosol optical properties can complement lidar observations by constraining aerosol-state-dependent LR near the surface and, where vertical representativeness is independently established, by supporting lower-boundary-layer lidar applications. ~~Recent studies have shown that aerosol optical properties and lidar ratio can be predicted or calculated from ground-based observations and then evaluated against Raman lidar retrievals, further highlighting the relevance of this connection (Liu et al., 2024; Eswaran et al., 2023).~~ In practical applications, LR is often simplified as a pre-assumed constant for elastic lidar retrievals. However, in complex mixed aerosol environments, its range of variation can expand significantly, thereby introducing uncertainties into retrieved extinction profiles and column-integrated aerosol optical depth (AOD) (Floutsi et al., 2023; Liu et al., 2024). In the atmosphere, LR can vary over a broad range of approximately 20–120 sr, depending strongly on aerosol type, wavelength, and absorption properties (Müller et al., 2007; Omar et al., 2009; Groß et al., 2013; Ohneiser et al., 2022). In particular, it is still challenging to obtain the LR at 1064 nm in most cases (Haarig et al., 2022; Wang et al., 2024). ~~The CALIPSO version 4 only provided an LR lookup table at 1064 nm for pure aerosol types (Kim et al., 2018), which does not exist within the atmospheric boundary layer.~~ CALIPSO Version 4 uses prescribed, subtype-

dependent lidar-ratio values for aerosol extinction retrievals (Kim et al., 2018), whereas lidar-ratio constraints representative of continuously varying mixed aerosols in the atmospheric boundary layer remain limited. AERONET Version 3 also provides multi-wavelength lidar ratios derived from column-integrated size distributions and complex refractive indices retrieved from Sun–sky radiance measurements ~~Although the LRs on multi-wavelengths are provided by AERONET version 3 inversion products, the CRIs have to be assumed or adopted from previous studies~~ (Shin et al., 2018). Such lidar-relevant optical parameters can be derived from *in situ* size distribution and absorption measurements, combined using Mie theory calculations under reasonable assumptions for CRIs. Combining a scanning mobility particle sizer (SMPS) with an optical particle counter (OPC) is a standard approach for constructing a continuous particle size distribution (PSD) from the nanometer to micrometer scale (Wiedensohler et al., 2012). Among representative in situ retrieval strategies, two approaches are particularly relevant. The first is the optical closure or iterative method, which utilizes concurrent observations from a nephelometer and an aethalometer to drive Mie model iterations to match the measured scattering and absorption coefficients (Mack et al., 2010). This approach provides strong physical constraints but demands highly specific instrument configurations. Furthermore, the filter tape multiple-scattering correction factor (often denoted as $C$) of the aethalometer frequently introduces additional uncertainties when dealing with complex absorbing aerosols (Backman et al., 2017; Zotter et al., 2017; Yus-Díez et al., 2021; Ferrero et al., 2024; Yus-Díez et al., 2025). The second is the geometric overlap method, which primarily relies on shape matching of SMPS and OPC data within their overlapping size region to retrieve $n$ (Hand and Kreidenweis, 2002; Vratolis et al., 2018; Zhao et al., 2019). This method is cost-effective and easy to deploy, but it fundamentally relies on geometric constraints. Lacking a direct constraint on the imaginary part $k$, it is more susceptible to ill-posed problems when processing absorbing mixed aerosols and is relatively sensitive to systematic sampling errors between instruments (Radney and Zangmeister, 2018; Frie and Bahreini, 2021). Moreover, recent studies show that the aerosol absorption coefficients and composition can be retrieved by lidar potentially (Li et al., 2026; Dong et al., 2026), which requires a bridge between lidar-relevant optical parameters and ground in situ observations. Unlike lidar retrievals, the standardized in situ aerosol microphysical and optical measurements are commonly performed under fixed low-RH conditions (ACTRIS, 2024). Consequently, hygroscopic growth changes of both particle size and the effective CRI (Flores et al., 2012), thereby affecting scattering, extinction, backscattering, SSA, and LR, must be accounted for when using in situ observations to constrain lidar-relevant products.

To integrate the advantages of these approaches while overcoming their respective limitations, this study proposes and demonstrates a decoupled inversion framework for deriving lidar-relevant aerosol optical products from in situ observations. The framework is composed of three sequential steps. In the first step, a physically continuous broad-spectrum PSD is reconstructed through Grimm-type OPC acceptance--angle response modelling (Heim et al., 2008; Walser et al., 2017) and geometric alignment in the overlap region, while the effective real refractive index at 655 nm is retrieved. In the second step, multi-wavelength absorption constraints and the singly subtractive Kramers–Kronig (SSKK) relation (Ohta and Ishida, 1988; Lucarini et al., 2005) are combined to retrieve spectrally consistent multi-wavelength CRIs and the associated SSA and LR. To further quantify the propagated impact of observational uncertainties, the framework also incorporates differentiated Monte

Carlo uncertainty sampling. By separating particle-size geometric remapping from absorption-driven optical closure, this framework is designed to reduce parameter coupling and to improve the physical consistency of the retrieved optical spectrum. The present framework also applies RH correction as a post-inversion forward calculation: the dry-state CRI retrieval is first obtained from the in situ PSD and absorption observations, and the lidar-relevant SSA and LR are then recalculated from an RH-adjusted PSD and a wet-state effective CRI with particle growth referenced to 40% RH ~~using the scattering enhancement factor, *f*(RH)~~ (Petters and Kreidenweis, 2007; Zieger et al., 2013). This step provides a physically consistent bridge between dry in situ-constrained retrievals and ambient lidar-relevant optical conditions.

Within this setting, this study develops and evaluates a three-stage decoupled framework for deriving dry-state homogeneous-equivalent CRI and RH-corrected lidar-relevant SSA and LR on triple wavelengths from in situ PSD, absorption, and RH observations, which aims to explore the wavelength-dependent characteristics of the SSA–LR parameter space and its implications for constraining lidar-related optical properties in the complex mixture of aerosol types. Specifically, the framework is used to reconstruct a response-corrected wide-range PSD, retrieve a spectrally consistent dry-state CRI anchored by $n_{655}$, assess the sensitivity of the optical products to the effective AE33 multiple-scattering correction factor, and examine the resulting wavelength-dependent SSA–LR parameter space. The framework is applied to observations from the Vipava Valley (Slovenia, Europe), a complex valley environment where near-surface aerosol size structure and absorption properties can vary substantially.

## 2~~.~~ Methodology

### 2.1 Study site and measurements

The measurement campaign was conducted from 7 to 23 April 2016 in the town of Ajdovščina (45.87° N, 13.91° E; 125 m a.s.l.; Figure 1), located in the center of the Vipava Valley in southwestern Slovenia. The site is representative of a near-surface valley environment in which aerosol conditions are influenced by both local accumulation and regional transport. Owing to the frequent coexistence of absorbing fine-mode background aerosol and episodic coarse-mode enhancement, the site provides a suitable test bed for evaluating retrieval performance under complex mixed-aerosol conditions (Wang et al., 2019).




**Figure 1. Topography and geographical location of the Ajdovščina measurement site in the Vipava Valley, Slovenia. Basemap © Google Maps. Map provided by Google Maps (https://www.google.com/maps, last access: 14 April 2026).**

~~Aerosol particle size distribution and absorption measurements were obtained from three in situ instruments deployed at the site: a scanning mobility particle sizer (SMPS), a Grimm-type optical particle counter (OPC, Model 1.109), and a multi-wavelength aethalometer (AE33). The SMPS provided the submicron particle number size distribution over approximately 10–1000 nm and was mainly used to constrain the fine-mode particle size distribution and the overlap-region matching with the OPC. The OPC measured particles over a nominal size range of 0.3–20 µm using a 655 nm internal laser and was used to characterize the coarse-mode distribution, with its response further accounted for in the subsequent instrument-specific retrieval.~~ Aerosol particle size distributions and absorption were measured through three separate sampling lines using a GRIMM SMPS+C system, a GRIMM 1.109 optical particle counter (OPC), and a multi-wavelength aethalometer (AE33). The SMPS+C, equipped with a long differential mobility analyzer (L-DMA) measured particle mobility size distributions over approximately 11–1083 nm. The GRIMM 1.109 OPC measured particles over a nominal size range of 0.3–20 µm using a 655 nm internal laser. The AE33 measured aerosol light absorption at seven wavelengths (370, 470, 520, 590, 660, 880, and 950 nm) and provided the absorption constraints required for the retrieval of the spectral imaginary refractive index and derived optical properties. The aerosol measurements used in the retrieval were referenced to low-humidity sampling conditions, and the data were averaged to 1 h to reduce short-term variability while retaining the principal temporal evolution. Additional details of the sampling configuration are provided in Supplement Sect. S1 and Table S1.

Within the retrieval framework, the SMPS measurements primarily constrained the fine-mode particle size distribution and the SMPS–OPC overlap-region matching with the OPC, whereas the OPC measurements constrained the coarse-mode contribution, with the instrument-specific optical response explicitly accounted for in the subsequent retrieval. The $PM_{2.5}$ and $PM_{10}$ values reported in this study are PSD-derived mass-equivalent diagnostics rather than independent gravimetric measurements. Similarly, eBC derived from the AE33 absorption record using the adopted $C_{eff}$ and $MAC_{880}$ was treated as a

diagnostic absorption-related quantity rather than an independent constraint on $C_{eff}$. A single-wavelength elastic lidar operating at 1064 nm was available during the campaign, but its Klett-type backscatter retrieval depends on an assumed lidar ratio and therefore provides no independent extinction or lidar-ratio reference, and no sun-photometer AOD dataset was available for the period. The retrieval products are therefore interpreted as internally consistent, site-specific, ambient-equivalent estimates rather than quantities independently validated against lidar or sun-photometer observations (see Sects. 4.1 and 4.3).

### 2.2 Decoupled retrieval framework

A decoupled geometric–optical retrieval framework was developed to derive spectrally consistent aerosol optical properties from combined SMPS, OPC, and AE33 observations (Figure 2). The framework consists of three sequential steps. In Step 1, the SMPS–OPC overlap region is used to reconstruct a physically continuous broad-spectrum particle size distribution and to retrieve the effective real refractive index at 655 nm. In Step 2, AE33-constrained absorption is combined with Mie calculations and an SSKK constraint to retrieve the spectral imaginary refractive index and the associated multi-wavelength optical properties. In Step 3, dry-state PSDs and CRIs are converted to ambient-equivalent wet optical properties using $\kappa$-Köhler hygroscopic growth (Zieger et al., 2013). The final outputs include the effective complex refractive index, extinction coefficient, scattering coefficient, backscatter coefficient, SSA, and LR at 355, 532~~, 655~~, and 1064 nm (Ohta and Ishida, 1988; Lucarini et al., 2005).

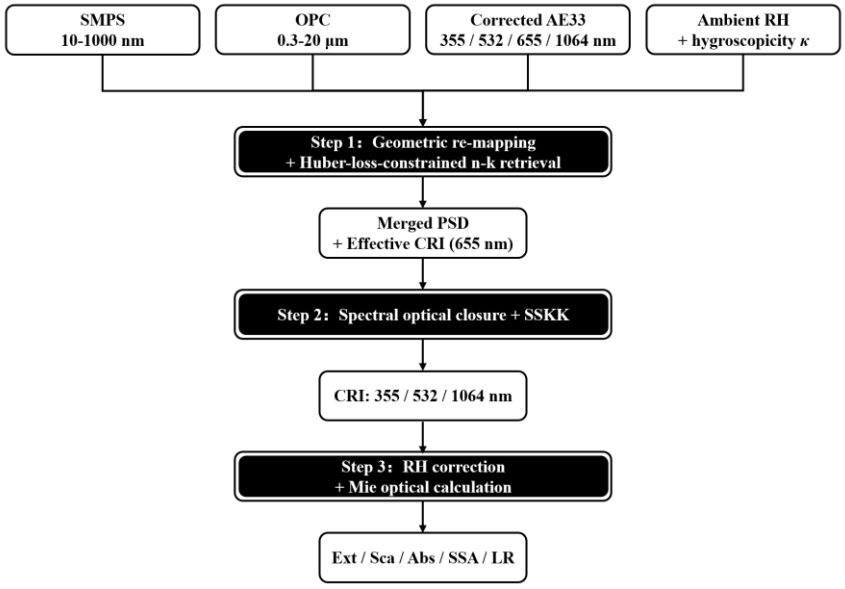

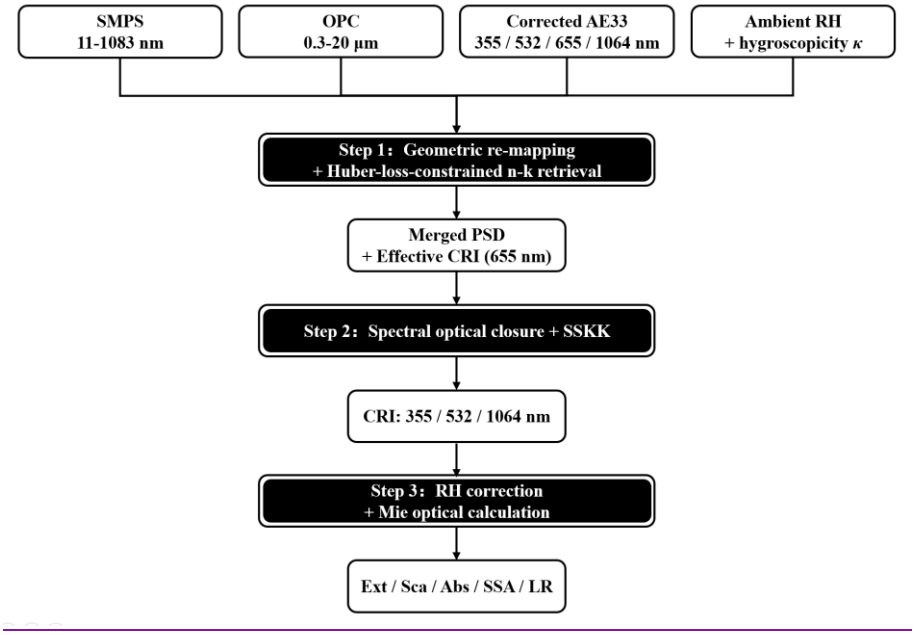


**Figure 2. Flowchart of the retrieval framework.**

### 2.2.1 OPC response modelling and lookup table construction

Since the Grimm 1.109 does not collect scattered light over the full solid angle, its response cannot be adequately represented by the total scattering efficiency integrated over 0°–180°. To account for this restricted acceptance geometry, the instrument response was modelled by integrating the single-particle Mie scattering signal over the effective collection-angle range adopted for the instrument-response calculation (Bemer et al., 1990; Heim et al., 2008; Walser et al., 2017):

$$Q_{\mathrm{sca,\ partial}}(D_p, m) = \frac{1}{x^2}\int_{\theta_{\min}}^{\theta_{\max}} \left(|S_1(\theta)|^2 + |S_2(\theta)|^2\right) w_{\mathrm{optics}}(\theta)\sin\theta \mathrm{d}\theta \qquad (1)$$

where $x$ = $\pi D_p/\lambda$ is the dimensionless Mie size parameter ~~incident wavelength (655 nm)~~, $D_p$ is the particle diameter, $\lambda$ = 655 nm is the OPC laser wavelength, $S_1(\theta)$ and $S_2(\theta)$ are the Mie scattering amplitude functions for the perpendicular and parallel polarization components respectively and $w_{\mathrm{optics}}(\theta)$ is a dimensionless relative angular-response weighting function ~~an empirical angular weighting function describing the optical collection efficiency of the instrument.~~. Following Heim et al. (2008), the integration interval was set to 30°–150°, and a weighting factor of 2.0 was assigned to the 81°–98° range, while a value of 1.0 was used for the remaining angular ranges. No additional normalization to unit integral or unit mean was applied.

To accelerate repeated calculations during the inversion, high-resolution lookup tables (LUTs) of scattering and absorption properties were precomputed. The real refractive index n ranged from 1.300 to 1.700 with a step size of 0.~~002~~001. The imaginary refractive index $k$ was logarithmically discretized into ~~50~~ 200 nodes from $10^{-5}$ to 0.6 (Dubovik and King, 2000).

The particle diameter $D_p$ ranged from 10 nm to 20 μm with 3000 logarithmically spaced nodes. Independent LUTs were constructed for 355, 532, 655, and 1064 nm.

### 2.2.2 Step 1: geometric alignment and PSD merging

The first step reconstructs a physically continuous PSD over 10 nm to 20 μm by combining the fine-mode SMPS distribution with the coarse-mode OPC measurements.

The effective complex refractive index at 655 nm ($m = n + ik$) was then retrieved using an alternating decoupled optimization scheme:

(1) given a prior value of $k$, the initial real refractive index $n_1$ was determined by minimizing a spectral-shape consistency objective function based on the Huber loss (Huber, 1964).

(2) using $n_1$, the initially merged PSD, and the absorption constraint at 655 nm, an intermediate optical closure was performed to obtain $k_1$.

(3) $k_1$ was substituted back into the geometric remapping module, and a high-resolution secondary search was carried out around $n_1$ to obtain the final retrieved real refractive index at 655 nm, $n_{655}$.

The SMPS distribution and OPC candidate distributions mapped under different trial $n$ values were interpolated onto a common logarithmic size grid over 350-750 nm. The intermediate 655 nm absorption closure feeds $k_1$ back into the remapping search. Therefore, the sStep -1 PSD and ~~$~~$n_{655655}$~~$~~$ estimates can depend indirectly on the assumed absorption correction. To emphasize spectral-shape consistency rather than absolute magnitude differences, residuals were de-meaned in logarithmic space, and the transition parameter of the Huber loss was set to $\delta$=0.5. ~~To quantify retrieval uncertainty, Monte Carlo framework was further applied. Instrument-specific random perturbations were simultaneously imposed on the SMPS, OPC, and absorption observations, and the standard deviations and 95 % confidence intervals of $n$, $k$, and the merged PSD were estimated from 500 independent retrieval realizations.~~To characterize the propagation of prescribed input perturbations through the retrieval framework, 500 Monte Carlo realizations were generated for each hourly retrieval. The resulting MC standard deviations and 2.5th–97.5th percentile ranges quantify the output spread associated with these perturbations. They represent the input-propagation component of retrieval uncertainty; structural and model-form sensitivities are evaluated separately as described in Sect. 2.3.

### 2.2.3 Step 2: AE33-constrained absorption closure and SSKK propagation

In the second step, the PSD reconstructed in Step 1 was combined with AE33-constrained absorption to retrieve the spectral imaginary refractive index and the associated multi-wavelength optical properties. The objective of this step was to obtain a

spectrally consistent complex refractive-index spectrum by coupling absorption closure with an SSKK constraint (Ohta and Ishida, 1988; Lucarini et al., 2005).

Aerosol absorption was derived from AE33 measurements at seven wavelengths (370, 470, 520, 590, 660, 880, and 950 nm). The absorption coefficients under the default AE33 multiple-scattering correction factor ($C_{default}$=1.57) were used as reference scenario~~baseline~~ input (Drinovec et al., 2015; Virkkula et al., 2015). To reconstruct the absorption coefficients at the retrieval wavelengths, the measured AE33 absorption spectrum was fitted using a constrained two-component power-law representation. This approach follows the general Aethalometer-model assumption that the measured absorption can be expressed as the sum of spectrally distinct absorbing components, each described by an absorption Ångström-type wavelength dependence (Sandradewi et al., 2008; Zotter et al., 2017). Here, the two fitted components are interpreted as BC-like and BrC-like spectral components, rather than as an independent quantitative source apportionment of BC and BrC.

$$\alpha_{abs}(\lambda) = \alpha_{BC,0}\left(\frac{\lambda}{\lambda_0}\right)^{-A_{BC}} + \alpha_{BrC,0}\left(\frac{\lambda}{\lambda_0}\right)^{-A_{BrC}} \quad (2)$$

where $\alpha_{BC,0}$ and $\alpha_{BrC,0}$ are the non-negative absorption amplitudes of the BC-like and BrC-like components at the reference wavelength $\lambda_0$; $A_{BC}$ and $A_{BrC}$ are the corresponding absorption Ångström exponents. The BC-like component represents weakly wavelength-dependent absorption, while the BrC-like component accounts for enhanced short-wavelength absorption. To improve component distinguishability and avoid instability in shortwave extrapolation, practical bounds of $0.7 \leq A_{BC} \leq 1.9$ and $3 \leq A_{BrC} \leq 10$ were imposed (Lack and Langridge, 2013). The fitted total absorption spectrum, rather than the individual component contributions, was then evaluated at 355, 532, 655, and 1064 nm and used as the absorption constraint in the refractive-index retrieval.

A sensitivity analysis of the AE33 multiple-scattering correction factor was further conducted within the retrieval framework (Di Biagio et al., 2017; Yus-Díez et al., 2021; Ferrero et al., 2024). Here, $C_{eff}$ was treated as a spectrally invariant scaling factor acting jointly across the full wavelength range within each time step. Accordingly, the target-wavelength absorption coefficients under different candidate $C_{eff}$ conditions were obtained by scaling the reference scenario~~baseline~~ spectrum proportionally:

$$\alpha_{abs,\,eff}(\lambda) = \alpha_{abs,\,default}(\lambda) \cdot \frac{C_{default}}{C_{eff}} \quad (3)$$

This treatment changes only the absolute magnitude of the absorption spectrum and preserves its relative spectral shape. Its applicability was subsequently evaluated through optical closure and physical consistency checks of the retrieved SSA and LR.

After parameterising $k(\lambda)$ from the AE33-constrained absorption, the corresponding real refractive-index spectrum was derived using the SSKK relation. Similar strategies have been applied in aerosol optical-constant retrievals to reduce truncation errors

arising from finite observational wavelength range (Wagner et al., 2021). The independently retrieved $n_{655}$ from Step 1 was used as the anchor value, and the SSKK equation was numerically solved over a finite integration window of [300, 35000] nm:

$$n(\lambda) = n(\lambda_{\text{anch}}) + \frac{2\left(\lambda_{\text{anch}}^2 - \lambda^2\right)}{\pi} \mathcal{P} \int_{\lambda_{\min}}^{\lambda_{\max}} \frac{\lambda' k(\lambda')}{\left(\lambda^2 - \lambda'^2\right)\left(\lambda_{\text{anch}}^2 - \lambda'^2\right)} \mathrm{d}\lambda' \qquad (4)$$

where $\lambda_{\text{anch}}$ = 655 nm is the anchor wavelength and P denotes the Cauchy principal value of the integral. The interval [300, 3000] nm represents a numerical integration window rather than an observational waveband; it was chosen to place the integration boundaries outside the target retrieval range (355–1064 nm), thereby reducing truncation effects from the unobserved shortwave and longwave tails. The retrieved $n(\lambda)$ and $k(\lambda)$ should therefore be interpreted as effective dry-state optical parameters of the sampled aerosol population. Under the present limited-waveband condition, the role of the SSKK constraint is to impose a physically consistent dispersion relationship on the retrieved refractive-index spectrum rather than to represent the full optical-constant spectrum of chemically pure materials.

### 2.2.4 Derivation of optical and microphysical properties

After obtaining the physically continuous PSD and the wavelength-dependent complex refractive indices, standard Mie theory was used to calculate the bulk aerosol optical properties, including the extinction coefficient, scattering coefficient, and backscatter coefficient (Bohren and Huffman, 1983). The framework provides a self-consistent set of wavelength-dependent bulk optical properties for subsequent interpretation and evaluation.

The single-scattering albedo and lidar ratio were then derived from the Mie-calculated optical coefficients as

$$SSA(\lambda) = \frac{\sigma_{\text{sca}}(\lambda)}{\sigma_{\text{ext}}(\lambda)} \qquad (5)$$

and

$$LR(\lambda) = \frac{\sigma_{\text{ext}}(\lambda)}{\beta_{\text{back}}(\lambda)} \qquad (6)$$

where $\sigma_{\text{sca}}(\lambda)$, $\sigma_{\text{ext}}(\lambda)$, and $\beta_{\text{back}}(\lambda)$ denote the bulk scattering, extinction, and volume backscatter coefficients, respectively. These intensive optical parameters were calculated at 355, 532 and 1064 nm and used as the primary lidar-relevant products. ~~To support the interpretation of aerosol-state-dependent structural variations, the effective radius was additionally calculated from the retrieved PSD as an auxiliary microphysical parameter (Hansen and Travis, 1974):~~

~~$$r_{\text{eff}} = \frac{\int D_p^3 \frac{dN}{d\log_{10} D_p} d\log_{10} D_p}{2\int D_p^2 \frac{dN}{d\log_{10} D_p} d\log_{10} D_p} \qquad (7)$$~~

### 2.2.5 RH correction for lidar-relevant optical products

To account for hygroscopic growth effects, RH correction was implemented as a post-inversion wet-state forward calculation applied to the dry-state homogeneous-equivalent retrieval products. This dry-to-ambient conversion follows the physical rationale of recent in situ–remote-sensing closure frameworks, in which dry in situ aerosol properties are transformed into humidified ambient-equivalent quantities for comparison with remote-sensing observations (Schlosser et al., 2025). Collocated hourly station RH was used as the near-surface ambient humidity input. Samples with RH > 95% were retained, but the RH used for hygroscopic-growth calculation was capped at 95% to avoid extrapolation beyond the parameterization range. The original RH values were preserved for quality control and identified separately. ~~excluded from the RH-corrected analysis to avoid near-saturation hygroscopic uncertainties and possible fog , cloud , or precipitation-related artefacts.~~ For RH < 40%, hygroscopic growth was assumed to be negligible, within the uncertainty of the adopted parameterization, and the retrieved aerosol properties were treated as an operational low-RH reference state. No additional water uptake was applied relative to this reference state (GF = 1). This treatment does not imply completely dry particles, but defines the low-RH observations as an operational reference state for subsequent RH-induced changes. For RH ≥ 40%, the measured RH was used to calculate the $\kappa$-Köhler growth factor, which was subsequently normalized to the 40% RH reference state.

~~with GF = 1, zero particle water volume fraction, and wet optical products equal to the corresponding dry products.~~ For 40% ≤ RH ≤ 95%, the measured RH was directly used in the $\kappa$-Köhler growth calculation without lower clipping to 40% (Petters and Kreidenweis, 2007).

Hygroscopic growth was parameterized separately for the fine and coarse modes using $\kappa_{\mathrm{fine}} = 0.20$ (representative of mixed continental/urban aerosols; e.g., Andreae and Rosenfeld, 2008; Pringle et al., 2010) and $\kappa_{\mathrm{coarse}} = 0.03$ (representative of relatively hydrophobic mineral dust; e.g., Koehler et al., 2009), with a fine–coarse split at $D_{\mathrm{p}} = 1$ μm. For each mode $s$, the RH-dependent growth relative to the selected low-RH reference state was expressed as

$$\sout{GF_s = \left(1+\kappa_s \frac{RH/100}{1-RH/100}\right)^{1/3}} \quad GF_{s,rel} = \frac{\left[1+\kappa_s RH/(100-RH)\right]^{1/3}}{\left[1+\kappa_s RH_{ref}/(100-RH_{ref})\right]^{1/3}} \quad (\sout{8}7)$$

where $RH$ and $RH_{\mathrm{ref}}$ are expressed in percent and $RH_{\mathrm{ref}} = 40\%$. The ambient-equivalent wet particle diameter was **~~obtained~~**then calculated as

$$\sout{D_{p,\mathrm{wet},s} = GF_s D_{p,\mathrm{dry},s}} \quad D_{p,\mathrm{wet},s}(RH) = GF_{s,rel} D_{p,ref,s} \quad (\sout{9}8)$$

where $D_{p,ref,s}$ denotes the particle diameter of mode $s$ at the selected 40% RH reference state, and $GF_{s,rel}$ is the corresponding reference-normalized growth factor defined in Eq. (7). Particle number in each reference-state size bin was conserved during the diameter transformation.

The wet homogeneous-equivalent complex refractive index was obtained by mixing the reference-state aerosol representation with the additional water associated with the RH increase, using the Bruggeman effective-medium approximation (Bruggeman, 1935). This quantity represents the effective refractive index of the aerosol–water mixture and is used only as an intermediate optical parameter in the RH-corrected forward calculation, rather than as the intrinsic CRI of the dry aerosol material. This distinction is important because aerosol water uptake changes both particle size and composition, and increasing water volume fraction generally lowers the real part of the effective refractive index and dilutes the absorbing aerosol material, while the resulting complex refractive index remains wavelength dependent (van Diedenhoven et al., 2022; Titos et al., 2021). The use of an effective-medium representation for internally mixed wet particles follows previous aerosol water-uptake and optical-closure applications (Flores et al., 2012).

The additional water volume fraction associated with growth relative to the reference state was estimated from the relative growth factor as

$$f_{w,s} = 1 - GF_{s,rel}^{-3} \quad (9)$$ ~~calculated growth factors.~~

The main RH-corrected products are the size-resolved homogeneous-equivalent wet optical properties relative to the selected low-RH reference state. Fine and coarse modes were humidified separately and evaluated with Mie theory (Bohren and Huffman, 1983) before summing their optical coefficients. Unless otherwise stated, all RH-corrected SSA and LR results refer to this homogeneous-equivalent wet forward calculation. The growth factor and paired LR response are continuous across the 40% operational reference, and omission of the 15 capped hours does not reverse the 1064-nm response.

## 2.3 Uncertainty characterization and structural assumptions

Variability and uncertainty were separated into campaign temporal variability, MC-propagated measurement-input uncertainty, deterministic structural sensitivity, and fixed/model-form assumptions (Table 1). Unless explicitly identified as MC-derived, the "±" values reported for the N = 304 cohort denote between-hour standard deviations and therefore describe temporal variability rather than retrieval uncertainty.

For each retained hour, 500 MC realizations were run using the instrument-specific mean-one lognormal perturbations listed in Table 1. SMPS bins and OPC channels were perturbed independently, AE33 inputs were perturbed independently by wavelength, and the instrument groups were mutually independent. MC summaries were calculated from realizations satisfying the predefined retrieval-validity criteria. The ensemble propagates measurement-input uncertainty only; structural choices were evaluated through deterministic sensitivity tests, whereas hygroscopicity, particle sphericity, and homogeneous-equivalent wet mixing remained fixed. Full perturbation and correlation specifications are provided in Supplement Sect. S3 and Table S4.

**Table 1. Classification and reporting of variability and uncertainty.**

| Category | Treatment | Interpretation / Reporting |
|---|---|---|
| Campaign temporal variability | Across-hour statistics for the post-QC cohort ($N$ = 304) | Mean ± SD and percentiles describe temporal variability, not retrieval uncertainty |
| MC-propagated input uncertainty | 500 mean-one lognormal realizations per retained hour: SMPS 10%, OPC 20%, and AE33 20% relative SD | MC SD and P2.5–P97.5 from valid realizations quantify input-propagation spread only |
| Deterministic structural sensitivity | Alternative $C_{eff}/C_{eff}(\lambda)$, overlap/remapping, concentration-offset, PSD-cutoff, and RH-treatment scenarios | Paired scenario-dependent changes; not confidence intervals |
| Fixed/model-form assumptions | Prescribed $\kappa_f$ = 0.2 and $\kappa_c$ = 0.03 were not sampled; spherical Mie; Bruggeman equivalent-medium treatment | Not probabilistically sampled; no total uncertainty estimate |

## 3 Results and technical evaluation

### 3.1 PSD reconstruction and synthetic closure of the decoupled retrieval framework

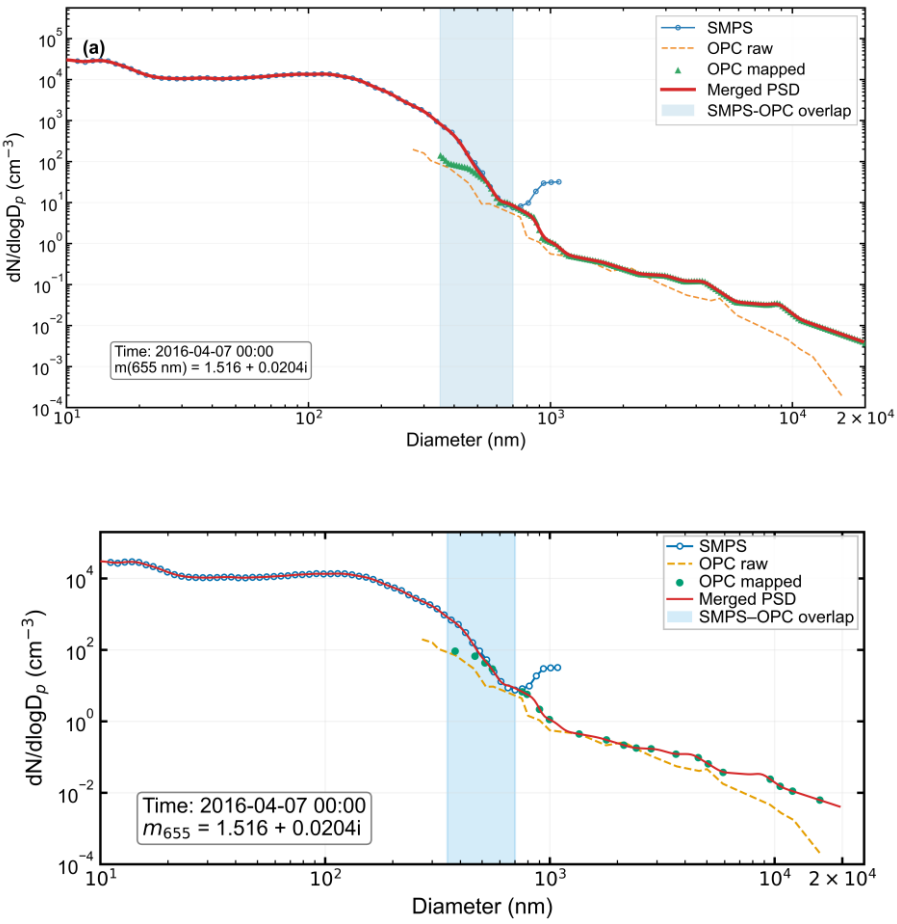


**Figure 3. Optical-size remapping and reconstruction of the dry continuous particle size distribution.**

Constructing a physically continuous PSD over the submicron-to-micron size range is a prerequisite for the subsequent optical retrieval. Figure 3 illustrates the response-constrained remapping of OPC optical-equivalent diameters onto a physical diameter coordinate and the subsequent merging with the SMPS size distribution. The remapping step is designed not only to reduce the geometric bias associated with OPC optical sizing, but also to retrieve the reference real refractive index, $n_{655}$, from spectral-shape consistency in the SMPS–OPC overlap region. Rather than directly merging the raw OPC optical-size spectrum, the OPC data are mapped onto candidate physical size coordinates using the instrument response model, and the optimal mapping

is selected using the overlap constraint. In the overlap region, approximately 350–750 nm, the remapped OPC spectrum shows improved consistency with the SMPS spectrum and yields a smoother transition in the reconstructed dry PSD. The reconstructed PSD and $n_{655}$ provide the basis for the subsequent absorption-constrained dry-state CRI retrieval and RH-corrected optical calculations.

A synthetic forward–inverse closure test was used to evaluate the numerical consistency of the retrieval framework under controlled conditions. Observation-informed PSD templates were combined with prescribed refractive-index inputs to generate the synthetic truth set. The test consisted of 12 representative PSD templates selected from the observational dataset and 40 prescribed spectrally consistent CRI states, giving $12 \times 40 = 480$ synthetic cases. Each case was forward-calculated into optical targets and then processed through the same retrieval pathway used for the observational analysis.

As shown in Figure 4, the retrieved $k$ and absorption coefficients were recovered with near-perfect numerical closure at all three wavelengths, with $R \approx 1.000$ and RMSE values on the order of $10^{-4}$. The real part $n$ also showed strong agreement with the prescribed truth ($R$ = 0.992–0.994), although its RMSE was larger, about 0.008–0.009. This difference indicates that the absorption-constrained branch is numerically stable, while the real refractive index retrieval remains more sensitive to the PSD remapping and OPC response assumptions.

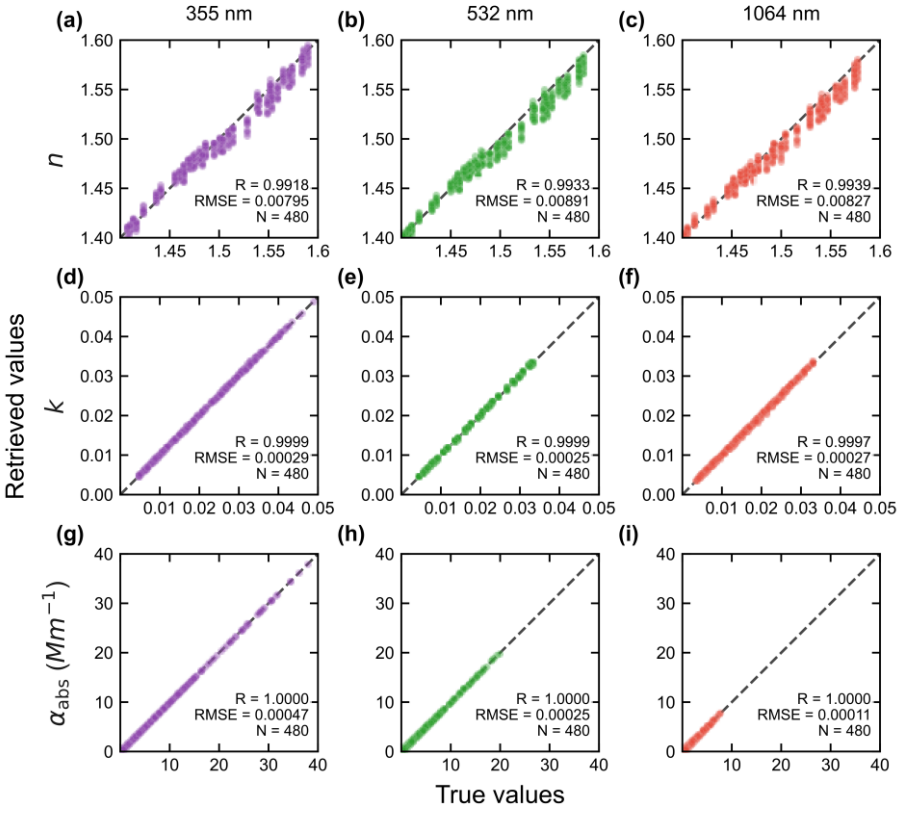


**Figure 4. Synthetic closure test of the decoupled retrieval framework using prescribed true and retrieved optical parameters.**

Overall, the synthetic closure test demonstrates the internal numerical consistency of the decoupled retrieval chain under controlled, internally consistent assumptions. It should therefore be interpreted as an algorithmic closure check rather than as an independent validation against an external atmospheric truth.

### 3.2 Absorption-correction sensitivity and reference scenario~~Absorption-correction sensitivity and baseline configuration~~

Unless otherwise stated, $n$ and $k$ denote the dry-state homogeneous-equivalent CRI retrieved from the in situ PSD and absorption observations, and are interpreted as material-like optical constraints for the sampled aerosol population. In contrast, $SSA_{RH}$ and $LR_{RH}$ denote RH-corrected, ambient-equivalent lidar-relevant products recalculated after RH-dependent particle growth. The wet-state effective CRI used in the optical calculation is treated as an intermediate aerosol–water mixture parameter rather than as the intrinsic CRI of the dry aerosol material. The corresponding wet–dry differences in SSA and LR are evaluated separately in Sect. 3.5.

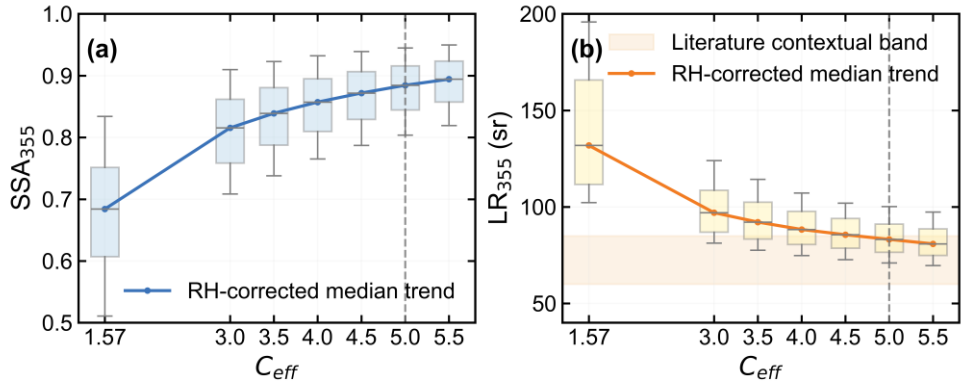


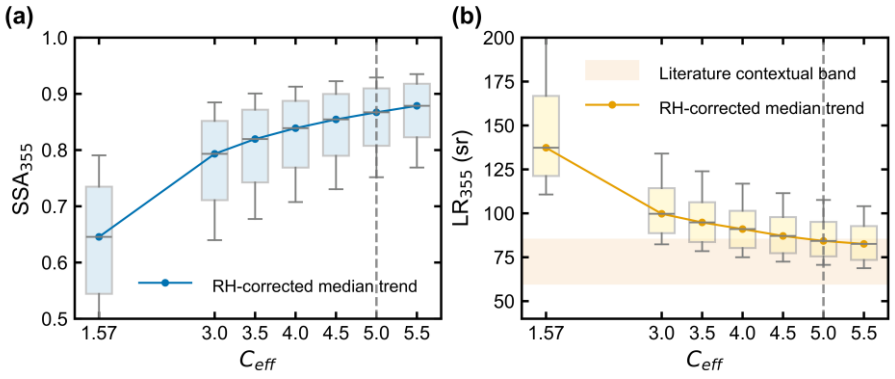


**Figure 5. Sensitivity of RH-corrected SSA and lidar ratio at 355 nm to the AE33 effective multiple-scattering correction factor, $C_{eff}$. Each boxplot represents the same post-QC hourly cohort ($N$ = 304). Boxplots show the sample distributions of SSA and LR at 355 nm for different $C_{eff}$ values, and markers connected by lines indicate the median trends. The shaded band in panel (b) denotes a literature-guided contextual~~plausibility~~ range for 355 nm LR, approximately 60–85 sr (Baars et al., 2012; Giannakaki et al., 2016).**

The sensitivity test examines the influence of the AE33 effective multiple-scattering correction factor, $C_{eff}$, on the absorption-constrained retrieval. Increasing $C_{eff}$ reduces the corrected absorption input and shifts the RH-corrected products toward higher $SSA_{355}$ and lower $LR_{355}$. Quantitatively, the median RH-corrected $SSA_{355}$ increased from 0.646 at $C_{eff}$ = 1.57 to 0.867 at $C_{eff}$ =5, while the median $LR_{355}$ decreased from 137.3 to 84.3 sr. At $C_{eff}$ = 5, the median $LR_{355}$ falls within the literature-guided contextual band of 60–85 sr. The literature range is shown for contextual comparison and is not used to calibrate $C_{eff}$, as no independent absorption reference is available to determine a unique value.~~, whereas the default correction setting remains well above this range.~~ This monotonic response demonstrates that the AE33 absorption correction is a dominant systematic control on absorption-sensitive lidar-relevant products.

The adopted ~~baseline~~ $C_{eff}$ = 5 reference scenario ~~-~~should be interpreted as a site- and period-specific effective correction setting rather than as an independently calibrated constant. Table ~~1~~ 2 places this choice in the context of reference-based AE33 correction studies, which show that $C$ depends on aerosol type, particle-size regime, and wavelength. Fine soot-like particles generally exhibit higher $C$ values, whereas mineral dust shows lower values; the Granada ambient case provides a mixed-aerosol reference with reported values of approximately 3.9–4.7 (Yus-Díez et al., 2025). The Vipava Valley aerosol population is also mixed, with substantial fine-mode contribution, but no independent absorption reference was available to determine a local $C_{eff}$. Therefore, both the literature values in Table ~~1~~ 2 and the shaded band in Figure 5b are used as contextual support for the sensitivity range ~~and baseline setting~~, not as direct calibration constraints or optimization targets.

The wavelength-dependent $C_{eff}(\lambda)$ sensitivity test preserved the campaign-level LR ordering and changed paired $LR_{1064}$ moderately, while hour-by-hour absorption ordering was less robust (Table S5; Figure S3).

**Table ~~1~~2. Literature context for AE33 multiple-scattering correction *C* and its relevance to the present sensitivity analysis.**

| Source | Aerosol type | Wavelength | Reported AE33 *C* | Relevance |
|---|---|---|---|---|
| Yus-Díez et al. (2025) | propane soot | 450/808 nm | 4.08/3.95 | Soot-like reference |
| | diesel soot | 450/808 nm | 6.25/5.27 | Fine soot-like upper reference |
| | mineral dust | 450 nm | 2.74–3.13 | Coarse/dust-like lower reference |
| | Granada ambient | 450/808 nm | 4.72/3.90 | Mixed ambient reference |
| This study | Vipava Valley mixed aerosol | 355/532/1064 | ~~Baseline~~ Reference case $C_{eff}$ = 5; sensitivity range 1.57–5.5 | Reference reporting scenario ~~Effective setting~~; Not independent calibration |

### 3.3 Reference scenario ~~Baseline~~ dry CRI and RH-corrected optical products

The fixed 385-hour analysis grid and the disposition of unavailable or screened hours are shown in Supplement Figure S1 and summarized in Table S2; Figure 6 displays the final post-QC optical-product cohort ($N$ = 304). Figure 6 first shows the retrieved dry-state homogeneous-equivalent CRI. The mean $n_{dry}$ values were 1.44~~98~~ ± 0.07~~65~~, 1.441 ± 0.075, and 1.43~~77~~ ± 0.07~~55~~ at 355, 532, and 1064 nm, respectively, indicating relatively weak spectral dispersion compared with the temporal variability. In contrast, $k_{dry}$ shows a clearer wavelength dependence, with mean values of 0.03~~09~~12 ± 0.013~~45~~, 0.023~~58~~ ± 0.009~~48~~, and 0.019~~02~~ ± 0.00~~75~~84 at 355, 532, and 1064 nm, respectively. The persistent ordering of $k_{355} > k_{532} > k_{1064}$ indicates stronger

short-wavelength absorption in the retrieved dry-state CRI.

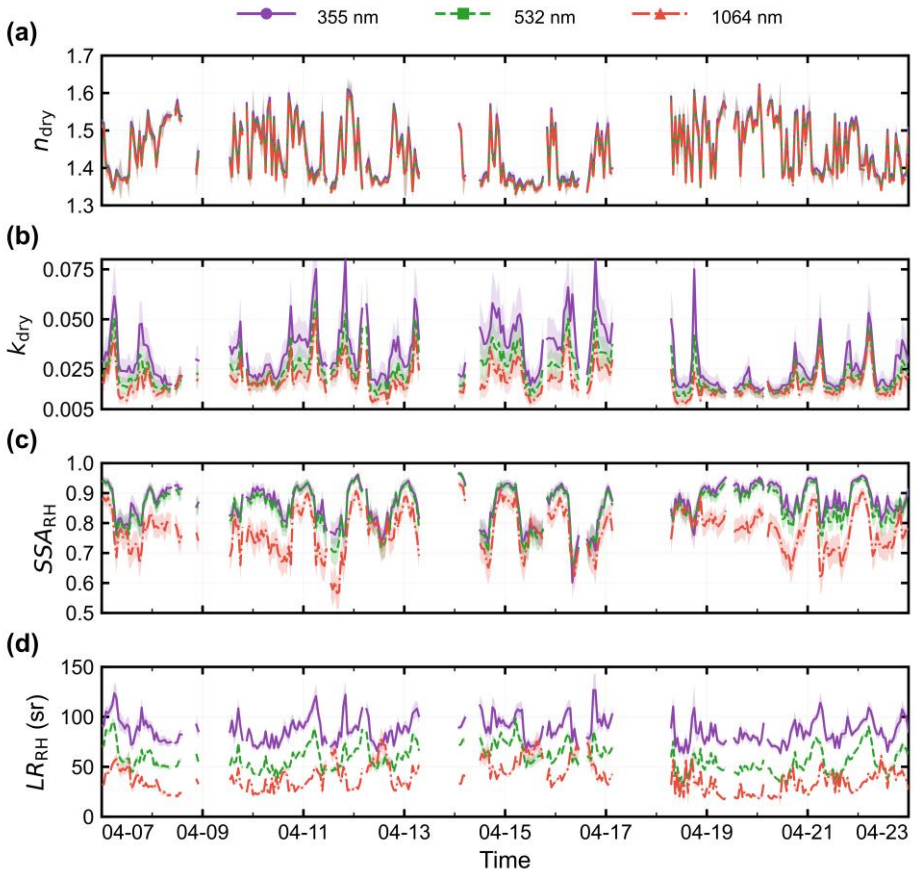


The lower panels show the RH-corrected SSA and LR recalculated from the RH-adjusted PSD and wet-state effective CRI. The RH-corrected mean SSA values were 0.85566 ± 0.0683, 0.84152 ± 0.07066, and 0.76074 ± 0.0731 at 355, 532, and 1064 nm, respectively. Although $k_{dry}$ is highest at 355 nm, $SSA_{355}$ remains close to $SSA_{532}$, indicating that the SSA spectrum is controlled not only by absorption but also by wavelength-dependent scattering efficiency. The lower $SSA_{1064}$ reflects the weaker long-wavelength scattering response and PSD-controlled Mie effects.

The corresponding mean LR values were 86.534 ± 13.822.7, 578.594 ± 12.805, and 39.812 ± 153.109 sr, decreasing by more than a factor of two from 355 to 1064 nm. This strong spectral decrease highlights the sensitivity of LR to the extinction-to-backscatter ratio, particularly through wavelength-dependent backscattering efficiency. Overall, Figure 6 establishes the reference scenario ~~baseline~~ dry-CRI-to-ambient-optics relationship: dry-state CRI provides the material-like optical constraint, while the final lidar-relevant SSA and LR are additionally shaped by PSD, RH-induced growth, and Mie backscattering.

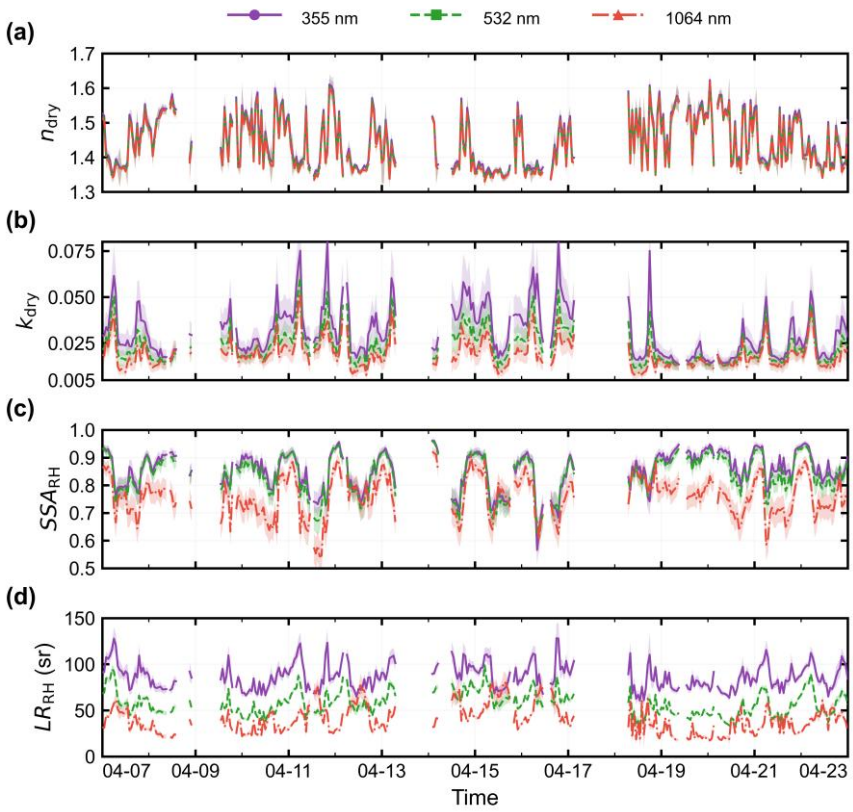


**Figure 6. Time series of dry-state equivalent CRI and RH-corrected lidar-relevant optical products. Panels show (a) $n_{dry}$, (b) $k_{dry}$, (c) $SSA_{RH}$, and (d) $LR_{RH}$ at 355, 532, and 1064 nm~~.~~ (*N* = 304). Shaded bands span the ± 1 SD range of the 500-realization Monte Carlo ensemble (input-propagation component only). Breaks mark hours excluded by the input, precipitation, loading, numerical, or post-retrieval ($n_{655}$ < 1.33) screens and are retained as gaps rather than interpolated.~~ Shaded bands indicate Monte Carlo retrieval uncertainty.~~**

Figure 7 shows that the dry-state CRI and RH-corrected lidar-relevant products exhibit coherent but wavelength-dependent diurnal variability. The real part $n_{dry}$ varies similarly at the three wavelengths, with only limited wavelength separation in the diurnal pattern~~suggesting that its diurnal variability is stronger than its spectral dispersion~~. In contrast, $k_{dry}$ shows a distinct early-morning increase around 05:00–07:00 LST, ~~with a persistent ordering of~~ $k_{355} > k_{532} > k_{1064}$ with generally stronger absorption at shorter wavelengths. ~~, indicating stronger short-wavelength absorption. The values of CRIs found in the study agree with the typical aerosol types within the valley, where the presence of dust and brown carbon aerosols caused higher absorption in the short wavelengths. The emission of carbonaceous aerosols in the region peaks at 6 a.m., mainly originating from motor vehicle activities and charcoal combustion for residential use, so the aerosols exhibit prominent light absorption characteristics overall. Industrial emissions dominate at noon, and inorganic components such as nitrates and sulfates account for the largest proportion of atmospheric aerosols, which show strong light scattering properties. In the evening, industrial~~

~~emissions, traffic and residential emission sources coexist and overlap, leading to a renewed sharp increase in carbonaceous aerosols and a decline of aerosol light absorption intensity to a moderate level. The temporal variation of observed aerosol optical parameters is highly consistent with the actual emission characteristics of the region.~~This feature indicates a temporal change in absorbing aerosol optical properties but does not uniquely identify a specific emission source. Independent SEM observations of campaign filter samples provide campaign-level evidence of irregular/mineral-like coarse particles, supporting the presence of heterogeneous aerosol components, but they are not used for hourly source attribution.

The RH-corrected optical products respond consistently to this absorption variability but are not controlled by absorption alone. $SSA_{RH}$ decreases during enhanced-absorption periods~~, while $LR_{RH}$ increases most clearly at 355 nm~~. The weaker coupling of 1064 nm with the shorter wavelengths indicates a stronger influence of particle-size-dependent Mie backscattering at the long wavelength. These results indicate that lidar-relevant SSA and LR benefit from temporally resolved and wavelength-dependent constraints, rather than from a single fixed empirical LR. The magnitude and wavelength dependence of the RH-induced transformation from dry to ambient-equivalent optical states are further examined in Sect. 3.5.

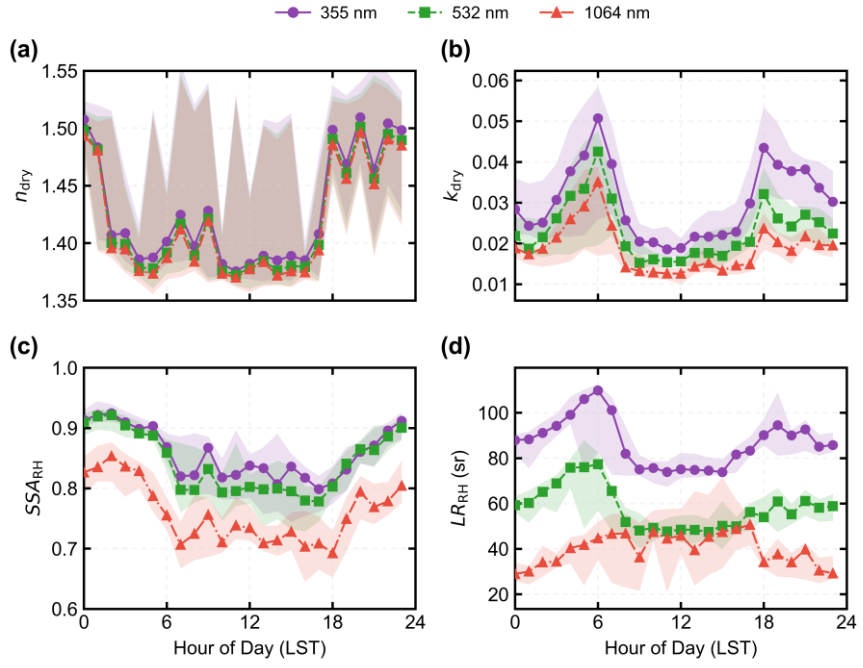

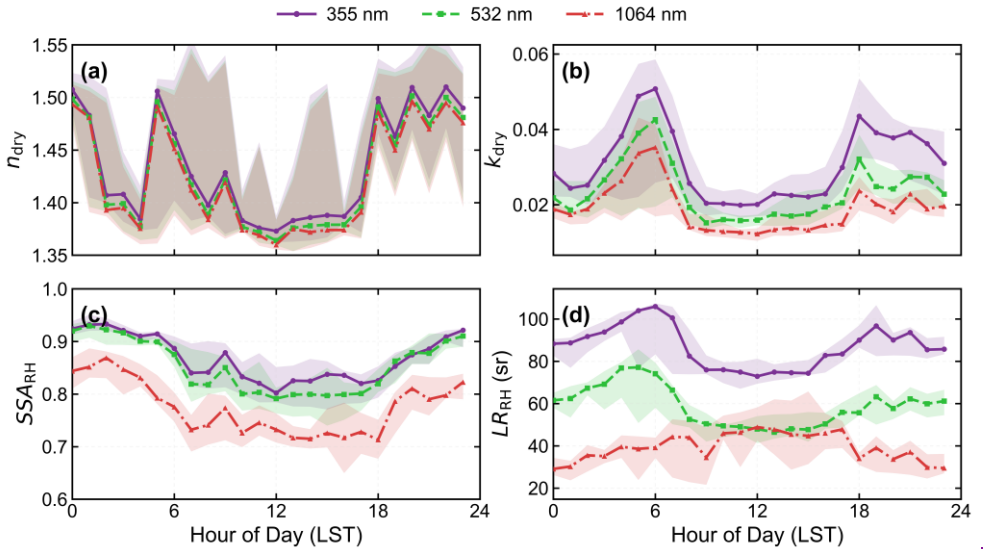


**Figure 7. Diurnal statistics of dry-state CRI constraints and RH-corrected lidar-relevant optical products at 355, 532, and 1064 nm. Panels show hourly statistics of (a) $n_{dry}$, (b) $k_{dry}$, (c) $SSA_{RH}$, and (d) $LR_{RH}$. Lines denote hourly median values, and shaded envelopes indicate the 25th–75th percentile range.**

### 3.4 Aerosol-regime dependence of lidar-relevant optical products

A secondary aerosol-state stratification using FVF and AAE was also examined. Within the analysed campaign, the broad FVF-related contrast in lidar ratio was retained under the tested wavelength-dependent absorption-correction scenario, whereas the detailed AAE-defined subclasses showed substantially greater classification sensitivity. The FVF–AAE groups are therefore interpreted only as diagnostic optical–microphysical groupings rather than fixed aerosol types or source classes. The full regime-resolved analysis is provided in Suppl. S7. Regime definitions and counts are given in Table S7; Figures S6–S9 show the temporal indicators, regime distributions, FVF-dependent median LR spectra, and $C_{eff}$ sensitivity, respectively.

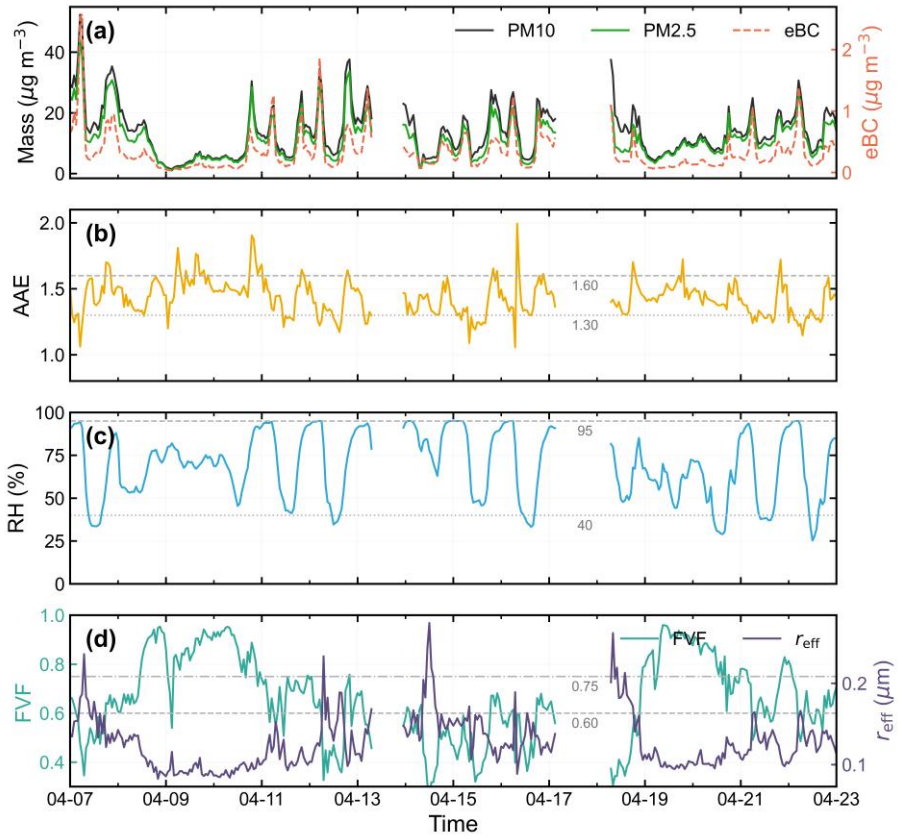


**Figure 8. Temporal evolution of optical microphysical indicators used to define aerosol diagnostic regimes. Panels show (a) $PM_{10}$, $PM_{2.5}$, and $eBC_{Ceff=5}$; (b) AAE(470/880); (c) relative humidity; and (d) FVF and effective radius. Horizontal reference lines indicate the RH and FVF thresholds used in the diagnostic classification.**

**Figure 8 provides the optical and microphysical context for the aerosol regime analysis. During the selected period, $PM_{10}$, $PM_{2.5}$ and eBC show substantial temporal variability, with median values of 12.5, 10.2 and 0.24 μg $m^{-3}$ respectively, and episodic maxima reaching 52.4, 44.0 and 2.57 μg $m^{-3}$. Several $PM_{2.5}$ enhancement periods coincide with elevated eBC, indicating increased absorbing aerosol loading during part of the campaign.**

**AAE ranges from 1.06 to 1.99, with a median of 1.43, showing that the samples cover different absorption spectral conditions. RH also varies widely, with an interquartile range of 53–88 %, indicating that the optical products were retrieved under substantially different humidity conditions. FVF spans from 0.26 to 0.96, while $r_{eff}$ ranges from 0.082 to 0.274 μm indicating that the dataset includes transitions between coarse-influenced, intermediate and fine-mode-**

~~dominated particle-size regimes. These variations provide the basis for using FVF and AAE as diagnostic optical–microphysical indicators.~~

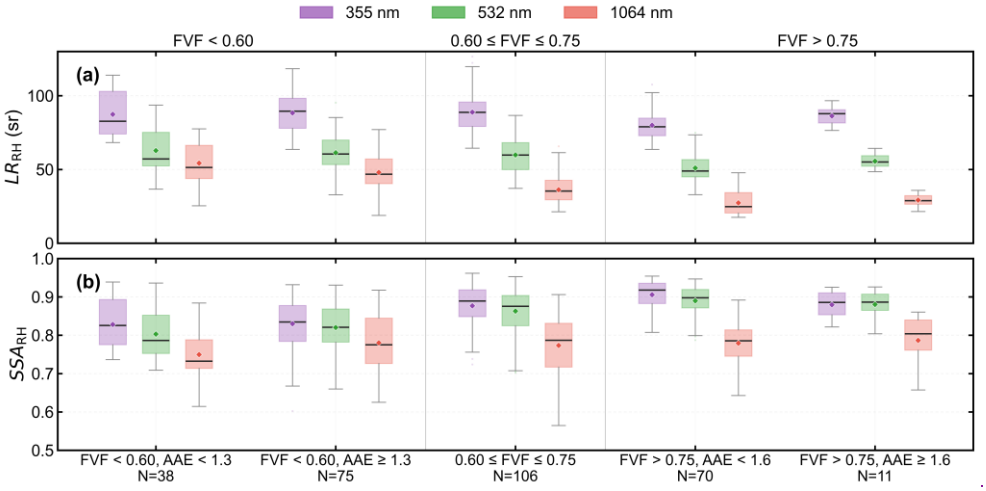


~~**Figure 9. Distributions of RH-corrected lidar ratio and SSA across FVF–AAE diagnostic regimes. Panels show (a) LR and (b) SSA at 355, 532, and 1064 nm. Aerosol regimes are defined using fine-mode volume fraction (FVF) and AAE(470/880).**~~

~~**Figure 9 shows that $LR_{RH}$ and $SSA_{RH}$ vary systematically across the FVF–AAE diagnostic regimes. Across all groups, the decrease of $LR_{RH}$ from 355 to 1064 nm agrees with the CALIPSO version 4, of which LR at 1064 nm is generally lower than at 532 nm (Kim et al., 2018). The separation among FVF regimes is especially evident at 1064 nm, indicating the importance of particle-size-controlled backscattering at the long wavelength.**~~

~~**The $SSA_{RH}$ increases from coarse-influenced to fine-mode-dominated conditions at all three wavelengths, with a stronger increase at 355 and 532 nm than at 1064 nm. This behaviour indicates that SSA is not controlled by absorption alone, but also by wavelength-dependent scattering efficiency and PSD effects. The AAE subdivision further modulates**~~

~~the optical products; the fine-mode high-AAE group retains a relatively high $LR_{355}$, consistent with stronger short-wavelength absorption.~~

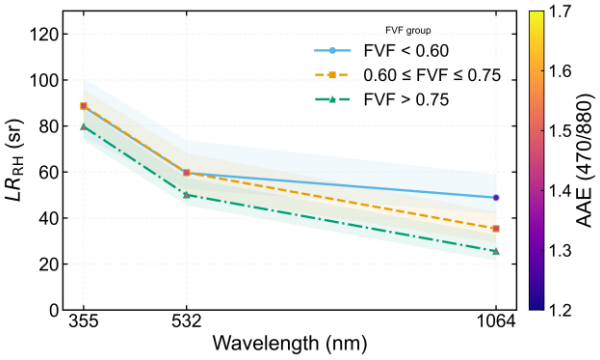


~~**Figure 10. FVF-dependent $LR_{RH}$ spectral profiles at 355, 532 and 1064 nm. Lines show the median LR values for each FVF regime, and shaded envelopes indicate the 25th–75th percentile range. Point colours indicate the distribution of AAE within each FVF regime and are used only as a qualitative indicator of absorption spectral variability.**~~

~~**Figure 10 further summarizes the FVF-dependent spectral profiles of RH-corrected lidar ratio. All FVF groups show decreasing $LR_{RH}$ from 355 to 1064 nm, but the magnitude of this decrease depends strongly on particle-size regime. For FVF < 0.60, the median $LR_{RH}$ values are 88.4, 59.6 and 48.9 sr at 355, 532 and 1064 nm, respectively, indicating a relatively flat LR spectrum. For FVF > 0.75, the corresponding values are 79.8, 50.1 and 25.6 sr, showing a much stronger decrease towards 1064 nm. Since this figure groups the data by FVF only, the AAE colour scale should be**~~

~~interpreted as a qualitative indication of absorption spectral variability rather than an independent quantification of the AAE effect.~~

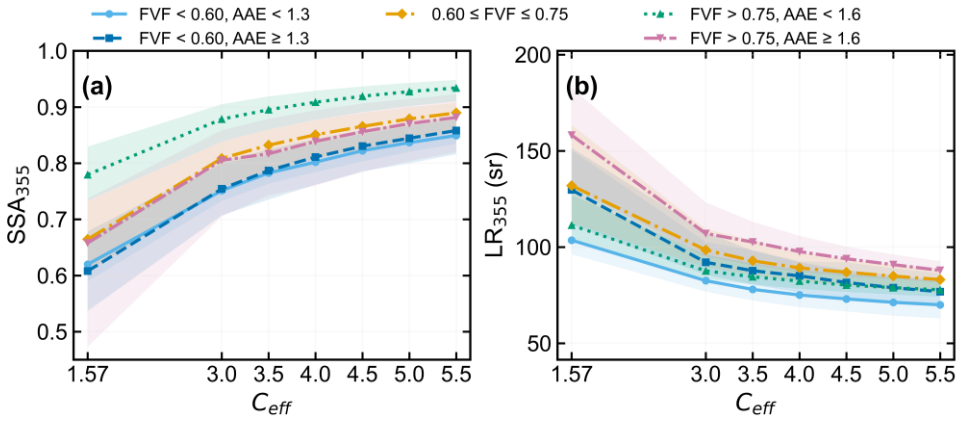


~~**Figure 11. Regime-dependent sensitivity of RH-corrected SSA and LR to $C_{eff}$. Panels show the sensitivity of (a) SSA and (b) $LR_{355}$ to the AE33 effective multiple-scattering correction factor $C_{eff}$ across FVF–AAE diagnostic regimes. Lines indicate regime median values, and shaded envelopes denote the 25th–75th percentile ranges.**~~

~~**Figure 11 shows that increasing $C_{eff}$ systematically increases $SSA_{355}$ and decreases $LR_{355}$ for all FVF–AAE regimes, reflecting the reduction in corrected AE33 absorption input. The response is strongest between $C_{eff}$=1.57 and 3.0 and becomes weaker at higher $C_{eff}$, indicating that the adopted baseline $C_{eff}$ lies in a relatively stable part of the sensitivity curve. The regime-dependent separation shows that the impact of the absorption-correction assumption is modulated by both particle-size structure and absorption spectral dependence. The fine-mode–lower-AAE regime retains the**~~

~~highest *SSA* and lowest $LR_{355}$, whereas the fine-mode high-AAE regime maintains higher $LR_{355}$, consistent with stronger short-wavelength absorption.~~

## 3.~~5~~ 5 Wavelength-dependent effects of RH correction on SSA and LR~~Effects of RH correction on SSA and LR~~

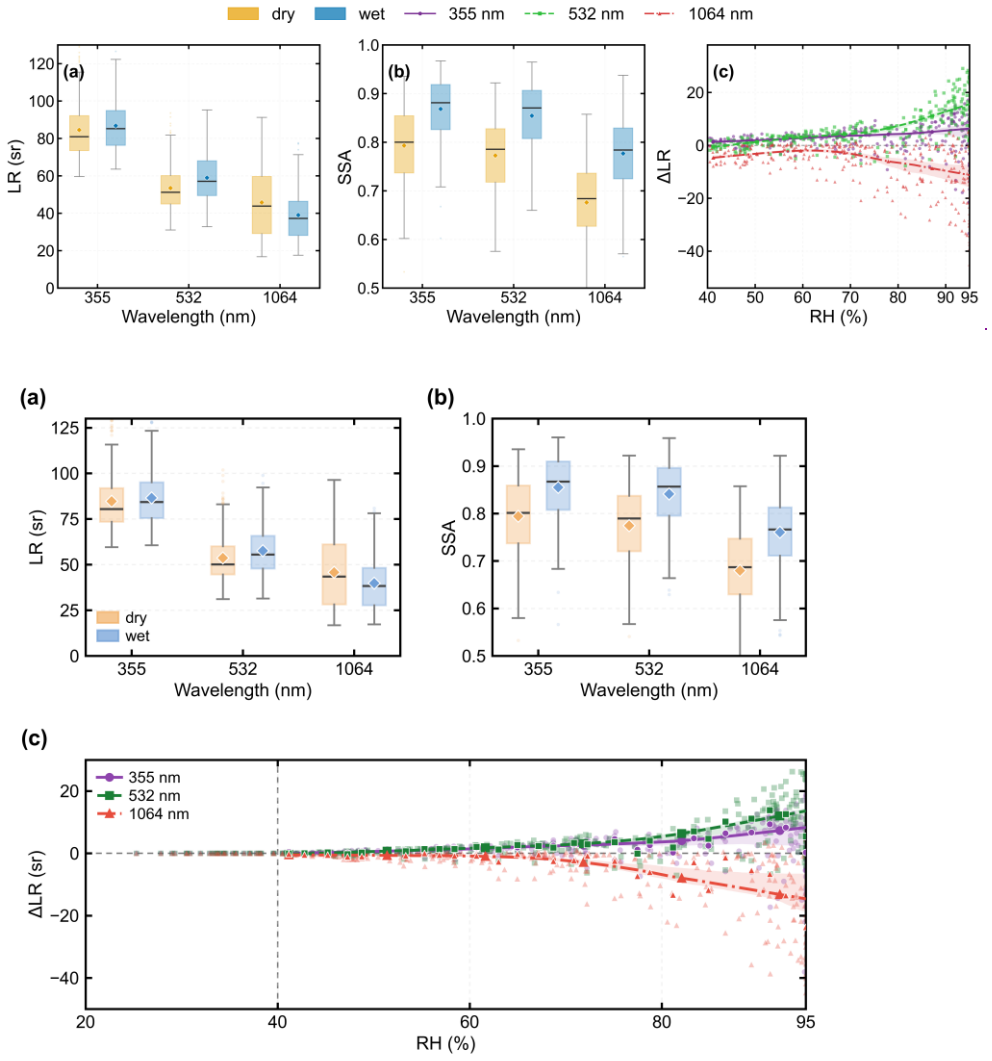


**Figure ~~12~~8. Effects of RH ~~-~~correction on SSA and lidar ratio for the RH-active subset ($N$ = 275). Panels show dry and RH-corrected (a) LR and (b) SSA at 355, 532, and 1064 nm, and (c) $\Delta LR = LR_{wet} - LR_{dry}$ as a function of RH. In panels (a) and (b), boxes indicate the interquartile range, horizontal lines indicate medians, and diamonds indicate means. In panel (c), points represent valid samples.**

Figure ~~12~~ 8 evaluates the effect of RH correction on lidar-relevant optical products for samples with RH ≥ 40%.~~,~~ The RH-corrected products were recalculated using RH-dependent particle growth, rather than by scaling the dry-state values. The

normalization and numerical continuity of the piecewise RH implementation around the 40% operational reference are documented in Figure S5a-b.

RH correction increases SSA at all wavelengths, with mean ΔSSA= $SSA_{wet} - SSA_{dry}$ values of 0.0687836, 0.074909, and 0.0891121 at 355, 532, and 1064 nm, respectively. In contrast, the LR response is wavelength dependent: mean ΔLR is positive at 355 and 532 nm (+2.0683 and +45.403 sr), but negative at 1064 nm (−6.6206 sr). This sign reversal indicates that hygroscopic growth modifies extinction and backscattering differently across wavelengths, highlighting the need to account for RH effects when dry in situ constraints are converted into ambient-equivalent lidar products.

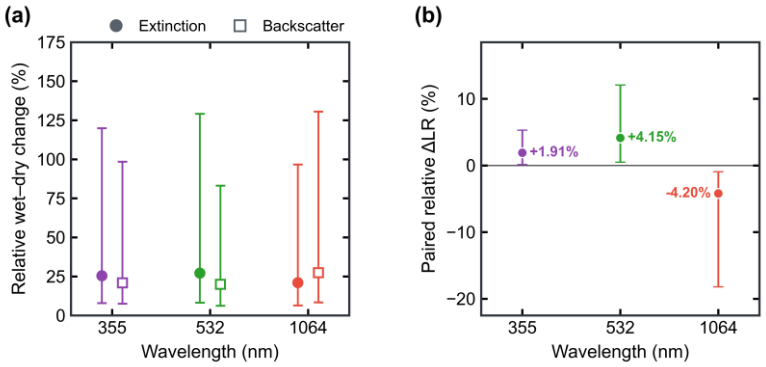


**Figure 9. Wavelength-dependent RH effects on aerosol optical properties. (a) Median relative changes in extinction and backscatter. (b) Median paired relative changes in lidar ratio. Markers and error bars denote medians and interquartile ranges, respectively, for the 275 RH-active hours.**

Figure 9 shows a wavelength-dependent RH response. The median relative extinction and backscatter changes were +25.44% and +20.94% at 355 nm, +27.14% and +19.93% at 532 nm, and +21.04% and +27.44% at 1064 nm. The LR change was calculated as an hourly paired relative change before aggregation; its medians were +1.91%, +4.15%, and −4.20%, respectively. ~~Figure 9 shows that the RH-induced optical response was wavelength-dependent but not monotonic with wavelength. At 355 and 532 nm, extinction increased more than backscatter (+25.44% versus +20.94% and +27.14% versus +19.93%, respectively), yielding median paired LR changes of +1.91% and +4.15%. At 1064 nm, the balance reversed: backscatter increased by +27.44%, compared with +21.04% for extinction, yielding a median paired LR change of −4.20%.~~ The 1064-nm LR decreased in 239 of 275 RH-active hours (86.9%). This response persisted after excluding the 15 RH-capped hours (226 of 260 hours; median change, −3.52%).

Hygroscopic growth modifies both particle size and the effective refractive index, thereby changing the size parameter and angular-scattering response across wavelengths. Previous studies have shown that hygroscopic effects on aerosol optical properties depend on particle size, composition, and wavelength (Titos et al., 2016). Wavelength-dependent hygroscopic effects have also been reported in multiwavelength lidar observations (Haarig et al., 2025). Within the coupled forward model used here, the sign of the LR response is determined by the relative changes in extinction and backscatter. At 1064 nm, the

larger relative enhancement of backscatter therefore produced a negative median LR response. However, the present analysis does not independently separate the contributions of particle-size growth and refractive-index change.

## 4 Discussion

### 4.1 Methodological implications and applicability boundaries

The methodological value of the framework lies in separating dry-state equivalent CRI constraints from ambient-equivalent lidar products, ~~-~~while keeping the two linked through physically constrained forward calculations. The $SSA_{RH}$ and $LR_{RH}$ used for lidar-oriented interpretation are subsequently obtained through RH-corrected forward optical calculations based on the RH-adjusted PSD and wet-state effective CRI. This sequential treatment keeps particle-size reconstruction, absorption-constrained CRI retrieval, and humidity correction as linked but distinct steps, thereby reducing direct parameter coupling under mixed-aerosol conditions. The synthetic forward–inverse experiment demonstrates algorithmic consistency under internally controlled assumptions, but it should not be interpreted as external atmospheric validation because the synthetic truth and retrieval share the same physical assumptions. Its main value is therefore to verify that the retrieval chain does not introduce numerical inconsistency when PSD, absorption, and dispersion constraints are mutually consistent.

The framework is therefore particularly useful for deriving local, physically constrained dry-state equivalent CRI and RH-corrected $SSA_{RH}$ and $LR_{RH}$ from in situ observations under mixed-aerosol conditions. These products provide aerosol-state-dependent optical constraints relevant to lidar applications~~can serve as lidar-relevant parameter constraints~~, especially when particle-size structure, absorption strength, and humidity-dependent optical response vary concurrently. Because the framework is constrained by near-surface in situ observations, its products are most directly applicable as local lidar constraints for near-surface or well-mixed lower-boundary-layer conditions, rather than as direct representations of the full vertically resolved aerosol column. Their practical role is therefore to constrain the optical state associated with the contemporaneous near-surface aerosol and to provide an observation-constrained basis for assessing whether assumed lidar-ratio values are locally consistent with that aerosol state. Extension beyond the near-surface layer requires evidence that the sampled aerosol is vertically representative. Where such representativeness can be established, the retrieved LR may provide an additional consistency constraint for lower-boundary-layer lidar retrievals, while the vertical aerosol structure must still be supplied independently. For radiative-transfer applications, the retrieved CRI and SSA constrain the local aerosol optical state, whereas column radiative-effect calculations additionally require vertically resolved or column-integrated aerosol loading information.~~The reliability of the retrieved products depends on the SMPS–OPC overlap quality, the assumed OPC response model, the AE33 absorption correction, and the prescribed hygroscopic-growth parameters.~~

### 4.2 Comparison with previous studies

Table 3 provides a contextual comparison of multi-wavelength LR values reported under different aerosol and observational conditions, with particular emphasis on the relatively scarce 1064-nm information. Because the studies differ in retrieval methodology, aerosol state, humidity treatment, and spatial representativeness, the comparison focuses primarily on reported spectral tendencies rather than direct agreement in absolute LR. Aerosol-type labels are retained only to describe the observational context reported in the original studies. ~~Table 2 places the present RH-corrected LR values in the context of representative lidar-related studies.~~ In the DeLiAn database compiled by Floutsi et al. (2023), the dust–smoke mixture category shows a decrease from 355 to 532 nm, which is qualitatively similar to the short-wavelength LR decrease retrieved here. Biomass-burning aerosol layers reported by Giannakaki et al. (2016) also show $LR_{355} > LR_{532}$, with high short-wavelength LR values partly overlapping the present $LR_{355}$ level, whereas their $LR_{532}$ is higher than the present mean value. As complementary algorithmic context, the CALIOP Version 4 retrieval scheme prescribes $LR_{532} > LR_{1064}$ for several continental and smoke-related aerosol subtypes, while assigning approximately wavelength-independent values to clean marine, dust, and dusty marine aerosols (Kim et al., 2018). These prescribed values are not direct multi-wavelength observations and are therefore used only as algorithmic context.

In contrast, the two observational studies in Table 3 that report 1064-nm LR show increasing central values toward 1064 nm, whereas the present campaign-level values decrease with wavelength. ~~In contrast, the two studies providing rare 1064-nm LR information show an opposite spectral behaviour.~~ Haarig et al. (2018) reported increasing LR values from 355 to 1064 nm for aged Canadian wildfire smoke in the 5–6.5 km tropospheric layer over Leipzig, and Wang et al. (2026) reported a similar increase for a night-time PBL aerosol case over Changsha. ~~These contrasting spectral behaviours may depend jointly on~~ These studies differ substantially in aerosol conditions, sampling altitude, humidity treatment, and retrieval methodology, preventing attribution of the spectral differences to any single factor ~~aerosol state, particle size distribution, particle shape, absorption spectral dependence, humidity state, vertical sampling, and retrieval context~~. Table 3 does not isolate the contribution of any individual factor to the inter-study differences. However, the limited number of direct multi-wavelength LR observations, particularly at 1064 nm, precludes identification of a universal spectral pattern.

The wavelength dependence of LR should also be interpreted within the broader context of aerosol optical complexity, because other optical properties such as SSA and absorption are likewise controlled by coupled effects of particle size, composition, and mixing state. ~~The non-universality of spectral behaviour is not limited to LR.~~ Recent size-resolved and core–shell-constrained studies have shown that SSA and absorption can vary nonlinearly across wavebands and cannot always be represented adequately by a single AAE or a simple monotonic spectral relationship (Guan et al., 2026a, b). Masoom et al. (2025) further reported non-monotonic SSA spectra and concave AOD spectral curvature in long-range-transported wildfire smoke, together with unusually large accumulation-mode particles and enhanced UV absorption. These findings provide broader support for the multi-wavelength constraints adopted here and caution against interpreting the retrieved SSA or LR spectra using a universal monotonic spectral assumption.

Therefore, the decreasing LR spectrum obtained in this study should be interpreted as a feature of the Vipava Valley near-surface, RH-corrected homogeneous-equivalent mixed aerosol state, rather than as a general lidar-ratio pattern. ~~This comparison supports the need for locally constrained in situ to lidar optical products instead of directly transferring fixed empirical LR spectra across aerosol types and sampling contexts.~~ The comparison further indicates that empirical LR values and assumed spectral relationships should be applied cautiously outside the aerosol and observational contexts from which they were derived.

**Table ~~2~~3. Contextual comparison of multi-wavelength lidar-ratio values from this study and representative previous lidar studies.**

| Study | Aerosol and sampling context | LR values |
|---|---|---|
| This study | Vipava Valley near-surface mixed aerosol; RH-corrected homogeneous-equivalent products constrained by in situ observations | $LR_{355/532/1064}$ = 86.5~~3~~4 ± 13~~2~~.82~~7~~ / 5~~7~~8.59~~4~~ ± 12.80~~5~~ / 39.81~~2~~ ± 15~~3~~.10~~9~~ sr |
| Floutsi et al. (2023) | Ground-based lidar database; dust–smoke mixture category | $LR_{355/532}$ = 72.1 ± 7.7 / 56.3 ± 6.5 sr |
| Kim et al. (2018) | CALIOP V4 operational retrieval algorithm; polluted continental/smoke subtype; prescribed LR values | $LR_{532/1064}$ = 70 ± 25 / 30 ± 14 sr |
| Giannakaki et al. (2016) | Biomass-burning aerosol layers observed by night-time multi-wavelength Raman lidar | $LR_{355/532}$ = 92 ± 10 / 75 ± 14 sr |
| Haarig et al. (2018) | Aged Canadian wildfire smoke over Leipzig; 5–6.5 km tropospheric layer | $LR_{355/532/1064}$ = 45 ± 5 / 68 ± 9 / 82 ± 27 sr |
| Wang et al. (2026) | Night-time PBL aerosol case over Changsha; below 3 km, PBL top about 2 km | $LR_{355/532/1064}$ = 45 ± 3 / 54 ± 9 / 65 ± 10 sr |

Values from previous studies are reported as given in the original publications, and the meaning of "±" follows the uncertainty or variability definition adopted in each source. For this study, values represent the campaign mean ± standard deviation of valid RH-corrected samples. Because uncertainty definitions, measurement/retrieval methods, aerosol and humidity conditions, and spatial representativeness differ among studies, Table 3 is intended for contextual comparison of reported LR magnitudes and spectral tendencies rather than direct validation of absolute values.~~The values are therefore intended for contextual comparison rather than direct uncertainty-equivalent validation.~~

### 4.3 Interpretation limits, uncertainty sources, and future work

Previous analyses of the broader 1–30 April 2016 Vipava campaign identified contrasting aerosol states, including Saharan-dust-influenced conditions during 11–18 April and predominantly locally influenced anthropogenic aerosol during 19–26 April, together with qualitative SEM–EDX evidence for mineral dust during the early-April dust episode (Wang et al., 2019). Subsequent lidar observations over the Vipava Valley reported aerosol states associated with mixtures of combustion-related aerosol, mineral dust, and marine aerosol under varying transport and meteorological conditions (Wang et al., 2022), while regional chemical studies identified sulfate-, ammonium-, and nitrate-containing fine aerosol as well as sea-salt-related

components in Slovenia and the northern Adriatic region (Turšič et al., 2006; Gluščić et al., 2020). The 2016 analysis therefore provides campaign-specific context, while the later studies provide broader regional context; none permits unique source attribution of the hour-resolved optical variability shown in Figure 7.

The FVF–AAE diagnostic regimes used in this study should be interpreted as optical–microphysical groupings for evaluating retrieval behaviour, rather than as a formal aerosol classification or source-apportionment scheme. The regimes are defined using FVF and $AAE_{470/880}$, while their interpretation is ~~supported~~ informed by complementary indicators, including eBC ~~corrected~~ calculated using $C_{eff}$ = 5, PM loading, RH, and $r_{eff}$, and therefore captures differences in particle-size structure and absorption-related optical behaviour. Detailed regime-resolved results are provided in Supplement Sect. S7, including the FVF-dependent LR spectra in Sect. S7.3 and Figure S8.

Within this interpretation framework, the regime-resolved $SSA_{RH}$ and $LR_{RH}$ distributions reflect the combined influence of wavelength, RH-adjusted particle-size structure, and the retrieved equivalent CRI, including its absorption spectral dependence. ~~show that the lidar-relevant optical response is controlled jointly by wavelength, absorption spectral dependence, RH-adjusted particle-size structure, and equivalent CRI.~~ For example, the coarse-influenced regime shows relatively high LR, especially at 355 nm, but this should not be interpreted as evidence of pure mineral dust. Rather, the relatively high LR is consistent with an influence of coarse-mode enhancement on the response-corrected PSD and the resulting optical properties, without implying a unique aerosol type or composition. The mode-decomposition analysis indicates that coarse-mode enhancement contributed to the higher $LR_{355}$, but differences remained in the fine-mode-only optical response (Supplement Sect. S7.5; ~~Fig.~~Figure S10). Similarly, the fine-mode high-AAE regime indicates a stronger wavelength dependence of absorption~~stronger absorption-related optical signatures~~, whereas the intermediate-FVF regime should be interpreted as a transition state between coarse-influenced and fine-mode-dominated particle-size conditions, rather than as a class-pure scattering-dominated regime. The $SSA_{RH}$–$LR_{RH}$ parameter space mapped onto dry-state CRI constraints further supports this interpretation by showing that dry-state absorption and refractive-index constraints partly structure the final RH-corrected lidar products, without implying a simple one-to-one aerosol-type classification.

The literature comparisons should therefore be used only as optical and instrumental context. Their purpose is not to validate the retrieved products against literature values, but to indicate where the RH-corrected $LR_{RH}$ values and the adopted $C_{eff}$ sensitivity range are positioned relative to previously reported aerosol optical states and reference-based AE33 correction factors. This distinction is important because most literature LR values are ambient, layer-resolved lidar products, whereas the present values are local RH-corrected equivalent products derived from retrievals constrained by in situ observations. Similarly, the AE33 $C$ values reported in reference-based studies are used to contextualize the sensitivity range and reference scenario ~~baseline~~ setting, not to prescribe a locally calibrated $C_{eff}$.

Several uncertainty sources require particular caution. First, the optical calculations rely on a spherical-particle, homogeneous-equivalent Mie representation. This assumption provides a tractable effective description of the sampled mixed aerosol population, but may introduce biases when coarse-mode or nonspherical particles make a substantial contribution (Huang et al., 2023).

PSD truncation lowered rather than raised $LR_{1064}$ and did not change the campaign-level LR ordering, although its magnitude remained sensitive to 2.5–10 μm support (Table S6; Figure S4). The retrieved CRI should therefore be interpreted as a homogeneous-equivalent optical parameter rather than a particle-resolved or composition-resolved refractive index. A related model-form uncertainty concerns the representation of aerosol mixing state. Recent studies using explicit core–shell constraints have shown that particle size, core-to-shell ratio, and coating assumptions can substantially modify multi-wavelength SSA and absorption estimates (Guan et al., 2026a, b). In contrast, the present framework retrieves a homogeneous-equivalent CRI designed to reproduce the bulk optical response of the sampled aerosol population. The bulk optical effects of possible absorbing cores, non-absorbing coatings, and externally mixed components are therefore represented only indirectly through the population-level homogeneous-equivalent CRI, rather than being resolved independently. This model-form difference may contribute to residual uncertainty in SSA and LR, but its magnitude and direction cannot be determined without a dedicated mixing-state sensitivity analysis. Second, the adopted $C_{eff} = 5$ should be interpreted as a site- and period-specific effective AE33 correction setting, not as a universal instrument constant. A systematic bias in the absorption input would affect the dry-state $k_{dry}$ retrieval and subsequently propagate into the RH-corrected SSA and LR. Third, RH correction relies on prescribed mode-dependent hygroscopicity parameters rather than direct HTDMA or CCNC measurements. The RH-corrected products should therefore be understood as ambient-equivalent forward estimates rather than independent wet-state observations. In addition, the wet-state calculation represents water uptake through particle growth and effective-medium mixing rather than an explicit core–shell coating geometry; morphology-dependent absorption enhancement or lensing effects are therefore not independently resolved.

A further limitation is vertical representativeness: the station-based PSD, absorption, and RH measurements directly constrain the near-surface aerosol state, so application of the retrieved LR to elevated or vertically heterogeneous layers requires independent information on aerosol vertical structure. ~~A further limitation is vertical representativeness: station-based PSD, absorption, and RH measurements may not fully represent the aerosol layer sampled by a vertically resolved lidar.~~

Overall, these limitations define the interpretation range of the framework rather than invalidating its purpose. The approach provides a practical solution for deriving multi-wavelength dry-state equivalent CRI and RH-corrected SSA and LR from in situ PSD, absorption, and RH observations under mixed-aerosol conditions. The present application should be viewed as an internally consistent, site-specific demonstration. Future applications at additional sites, supported by independent optical, chemical, hygroscopicity, particle-shape, and vertically resolved lidar constraints, will be needed to assess the broader transferability of the framework.

## 5 Conclusions

Based on in situ SMPS, OPC, AE33, and ambient RH observations, this study developed a decoupled framework for deriving dry-state homogeneous-equivalent CRI and RH-corrected lidar-relevant SSA and LR in the near-surface mixed-aerosol environment of the Vipava Valley. The framework reconstructs a response-corrected wide-range PSD, retrieves the reference

real part $n_{655}$, derives a spectrally consistent dry-state CRI using absorption and SSKK constraints, and recalculates SSA and LR through an RH-corrected wet-state forward calculation.

The RH-corrected LR values fall within the range of values reported under several mixed and biomass-burning-influenced observational contexts~~overlap the broad range reported for mixed and biomass-burning-influenced aerosol states~~ in previous lidar studies, while the retrieved CRI and SSA provide complementary local optical constraints for the Vipava Valley aerosol population. The present $LR_{355} > LR_{532} > LR_{1064}$ behaviour is qualitatively consistent with the short-wavelength decrease reported for some mixed or biomass-burning aerosol layers, but contrasts with the limited number of 1064 nm lidar observations showing increasing LR toward 1064 nm for aged wildfire smoke and a PBL aerosol case. This contrast indicates that multi-wavelength LR spectral behaviour is not universal, but depends on aerosol state, particle-size distribution, particle shape, absorption spectral dependence, humidity state, vertical sampling, and retrieval assumptions.

The sensitivity analysis demonstrated that the assumed AE33 effective multiple-scattering correction is a major structural control on absorption-sensitive products. In the absence of an independent absorption reference, no unique $C_{eff}$ could be identified from the campaign data; the $C_{eff}$ = 5 results are therefore reported as a reference scenario~~The sensitivity analysis identified $C_{eff}$=5 as a plausible site- and period-specific AE33 correction setting~~. Regime-based diagnostics revealed systematic differences in RH-corrected SSA and LR across the FVF–AAE groupings, with additional variation associated with absorbing-particle loading, while the diagnostic regimes should be interpreted as optical–microphysical states rather than source-apportioned aerosol classes. RH correction increased SSA at all three wavelengths and produced wavelength-dependent LR changes, highlighting the need to account for humidity when dry products constrained by in situ observations are compared with ambient lidar-relevant optical conditions.

Overall, the framework provides a physically constrained pathway for linking dry in situ CRI retrievals with RH-corrected multi-wavelength aerosol optical products relevant to lidar applications. These conclusions should be interpreted within several caveats, including the assumption of spherical particles and a homogeneous-equivalent representation of aerosol mixing state, the site- and period-specific $C_{eff}$=5 AE33 correction setting, the use of prescribed mode-dependent $\kappa_{fine}$ and $\kappa_{coarse}$ values for RH correction, and the limited vertical representativeness of near-surface in situ observations.

Future work should combine this framework with independently calibrated absorption measurements, nephelometer scattering closure, chemical composition constraints, direct hygroscopicity measurements, particle-depolarization information, and collocated Raman or HSRL profiles. Such integrated measurements would help further validate the framework and assess its broader transferability across different aerosol environments.

## Code and data availability

The source code of the VIPAVA Inversion Pipeline and the processed input data have been deposited in Zenodo (Yao et al., 2026). The record is currently under restricted access for peer-review purposes, and access is provided to the editor and reviewers. The record will be made publicly available upon publication.

## Author contributions

All the authors made contributions to this research work and manuscript. In particular, CY and LW designed the overall strategy of this work. MBM, LD, AG, FG, JV, MM, MG, GM, and SS organized the observation campaign, with MG, GM, and SS further participating in field observations and data collection. CY, AH, BZ, ZY and LW participated in the data analysis. CY wrote the initial manuscript draft. CY, LW, LD, AG and GM participated in the scientific discussions, reviewed, and proofread the manuscript. LW, FG, DC, and GM acquired the research funding and supervised the study. All authors have read and agreed to the published version of the manuscript.


## Financial support

This work was supported by the National Natural Science Foundation of China (grant Nos. 42475147 and 42575146), the Key Program of National Natural Science Foundation of China (42530112), the Jinhua Science and Technology Plan Project (Grant No. 2026-3-002), the ARIS programs P1-0385, I-0033 and project L1-4386, and the High-Performance Computing Center of Zhejiang Normal University.


## Competing interests

The authors declare no conflict of interest.

## References


ACTRIS: ACTRIS Standard Procedures for In situ Aerosol Sampling, Measurements, and Analyses at ACTRIS Observatories, Version 1.0, ACTRIS-ERIC, Center for Aerosol In situ Measurement and European Center for Aerosol Calibration and Characterization (CAIS-ECAC), available at: https://www.actris-ecac.eu/files/ACTRIS_standard_procedures_for_aerosol_in-situ_measurements.pdf, last access: 10 June 2026, 2024.

Andreae, M. O., and Rosenfeld, D.: Aerosol–cloud–precipitation interactions. Part 1. The nature and sources of cloud-active aerosols, Earth-Sci. Rev., 89, 13–41, https://doi.org/10.1016/j.earscirev.2008.03.001, 2008.

Baars, H., Ansmann, A., Althausen, D., Engelmann, R., Heese, B., Müller, D., Artaxo, P., Paixao, M., Pauliquevis, T., and Souza, R.: Aerosol profiling with lidar in the Amazon Basin during the wet and dry season, J. Geophys. Res.-Atmos., 117, D21201, https://doi.org/10.1029/2012JD018338, 2012.

Backman, J., Schmeisser, L., Virkkula, A., Ogren, J. A., Asmi, E., Starkweather, S., Sharma, S., Eleftheriadis, K., Uttal, T., Jefferson, A., Bergin, M., Makshtas, A., Tunved, P., and Fiebig, M.: On aethalometer measurement uncertainties and an instrument correction factor for the arctic, Atmos. Meas. Tech., 10, 5039–5062, https://doi.org/10.5194/amt-10-5039-2017, 2017.

Bemer, D., Fabries, J. F., and Renoux, A.: Calculation of the theoretical response of an optical particle counter and its practical usefulness, J. Aerosol Sci., 21, 689–700, https://doi.org/10.1016/0021-8502(90)90123-F, 1990.

Böckmann, C., Ritter, C., and Graßl, S.: Improvement of aerosol coarse-mode detection through additional use of infrared wavelengths in the inversion of Arctic lidar data, *Remote Sens.*, 16, 1576, https://doi.org/10.3390/rs16091576, 2024.

Bohren, C. F. and Huffman, D. R.: *Absorption and Scattering of Light by Small Particles*, Wiley, New York, ISBN 978-0-471-29340-8, 1983.

Bond, T. C., Doherty, S. J., Fahey, D. W., Forster, P. M., Berntsen, T., DeAngelo, B. J., Flanner, M. G., Ghan, S., Kärcher, B., Koch, D., Kinne, S., Kondo, Y., Quinn, P. K., Sarofim, M. C., Schultz, M. G., Schulz, M., Venkataraman, C., Zhang, H., Zhang, S., Bellouin, N., Guttikunda, S. K., Hopke, P. K., Jacobson, M. Z., Kaiser, J. W., Klimont, Z., Lohmann, U., Schwarz, J. P., Shindell, D., Storelvmo, T., Warren, S. G., and Zender, C. S.: Bounding the role of black carbon in the climate system: a scientific assessment, J. Geophys. Res.-Atmos., 118, 5380–5552, https://doi.org/10.1002/jgrd.50171, 2013.

Bruggeman, D. A. G.: Berechnung verschiedener physikalischer Konstanten von heterogenen Substanzen. I. Dielektrizitätskonstanten und Leitfähigkeiten der Mischkörper aus isotropen Substanzen, Ann. Phys., 416, 636–664, https://doi.org/10.1002/andp.19354160705, 1935.

Chen, A., Zhao, C., and Fan, T.: Spatio-temporal distribution of aerosol direct radiative forcing over mid-latitude regions in north hemisphere estimated from satellite observations, Atmos. Res., 266, 105938, https://doi.org/10.1016/j.atmosres.2021.105938, 2022.

Cheng, Y., Liu, C., Wang, J., Wang, J., Zhang, Z., Chen, L., Ge, D., Zhu, C., Wang, J., and Ding, A.: An observation-constrained estimation of brown carbon aerosol direct radiative effects, Atmos. Chem. Phys., 24, 3065–3078, https://doi.org/10.5194/acp-24-3065-2024, 2024.

Di Biagio, C., Formenti, P., Cazaunau, M., Pangui, E., Marchand, N., and Doussin, J.-F.: Aethalometer multiple scattering correction Cref for mineral dust aerosols, Atmos. Meas. Tech., 10, 2923–2939, https://doi.org/10.5194/amt-10-2923-2017, 2017.

Dong, Q., Huang, Z., Liu, Q., Wang, Y., Li, Z., Bi, J., Zhou, T., and Shi, J.: High-resolution profiling of aerosol absorption coefficients using dual-polarization lidar and a PSO–GPR machine learning approach, Opt. Express, 34, 4418–4431, https://doi.org/10.1364/OE.587704, 2026.

Drinovec, L., Močnik, G., Zotter, P., Prévôt, A. S. H., Ruckstuhl, C., Coz, E., Rupakheti, M., Sciare, J., Müller, T., Wiedensohler, A., and Hansen, A. D. A.: The "dual-spot" aethalometer: an improved measurement of aerosol black carbon with real-time loading compensation, Atmos. Meas. Tech., 8, 1965–1979, https://doi.org/10.5194/amt-8-1965-2015, 2015.

Dubovik, O. and King, M. D.: A flexible inversion algorithm for retrieval of aerosol optical properties from Sun and sky radiance measurements, J. Geophys. Res.-Atmos., 105, 20673–20696, https://doi.org/10.1029/2000JD900282, 2000.

Elsey, J., Bellouin, N., and Ryder, C.: Sensitivity of global direct aerosol shortwave radiative forcing to uncertainties in aerosol optical properties, *Atmos. Chem. Phys.*, **24**, 4065–4081, https://doi.org/10.5194/acp-24-4065-2024, 2024.

Eswaran, K., Montoux, N., Chauvigné, A., Baray, J.-L., Ancellet, G., Sellegri, K., Freney, E., Rose, C., and Pelon, J.: Lidar ratio calculations from in situ aerosol optical, microphysical and chemical measurements: Observations at puy de Dôme, France and analysis with CALIOP, Atmos. Res., 296, 107043, https://doi.org/10.1016/j.atmosres.2023.107043, 2023.

Ferrero, L., Losi, N., Rigler, M., Gregorič, A., Colombi, C., D'Angelo, L., Cuccia, E., Cefalì, A. M., Gini, I., Doldi, A., Cerri, S., Maroni, P., Cipriano, D., Markuszewski, P., and Bolzacchini, E.: Determining the aethalometer multiple scattering enhancement factor C from the filter loading parameter, Sci. Total Environ., 917, 170221, https://doi.org/10.1016/j.scitotenv.2024.170221, 2024.

Floutsi, A. A., Baars, H., Engelmann, R., Althausen, D., Ansmann, A., Bohlmann, S., Heese, B., Hofer, J., Kanitz, T., Haarig, M., Ohneiser, K., Radenz, M., Seifert, P., Skupin, A., Yin, Z., Abdullaev, S. F., Komppula, M., Filioglou, M., Giannakaki, E., Stachlewska, I. S., Janicka, L., Bortoli, D., Marinou, E., Amiridis, V., Gialitaki, A., Mamouri, R.-E., Barja, B., and Wandinger, U.: DeLiAn – a growing collection of depolarization ratio, lidar ratio and ångström exponent for different aerosol types and mixtures from ground-based lidar observations, Atmos. Meas. Tech., 16, 2353–2379, https://doi.org/10.5194/amt-16-2353-2023, 2023.

Flores, J. M., Bar-Or, R. Z., Bluvshtein, N., Abo-Riziq, A., Kostinski, A., Borrmann, S., Koren, I., Yinon, L., and Rudich, Y.: Absorbing aerosols at high relative humidity: linking hygroscopic growth to optical properties, Atmos. Chem. Phys., 12, 5511–5521, https://doi.org/10.5194/acp-12-5511-2012, 2012.

Frie, A. L. and Bahreini, R.: Refractive index confidence explorer (RICE): a tool for propagating uncertainties through complex refractive index retrievals from aerosol particles, Aerosol Sci. Technol., 55, 703–717, https://doi.org/10.1080/02786826.2021.1895428, 2021.

Giannakaki, E., van Zyl, P. G., Müller, D., Balis, D., and Komppula, M.: Optical and microphysical characterization of aerosol layers over South Africa by means of multi-wavelength depolarization and Raman lidar measurements, Atmos. Chem. Phys., 16, 8109–8123, https://doi.org/10.5194/acp-16-8109-2016, 2016.

Gluščić, V., Čačković, M., Pehnec, G., and Bešlić, I.: Ionic composition of $PM_{2.5}$ particle fraction at a coastal urban background site in Croatia, Atmos. Pollut. Res., 11, 2202–2214, https://doi.org/10.1016/j.apr.2020.07.004, 2020.

Groß, S., Esselborn, M., Weinzierl, B., Wirth, M., Fix, A., and Petzold, A.: Aerosol classification by airborne high spectral resolution lidar observations, *Atmos. Chem. Phys.*, **13**, 2487–2505, https://doi.org/10.5194/acp-13-2487-2013, 2013.

Guan, L., Cohen, J. B., Wang, S., Tiwari, P., Liu, Z., Li, Z., and Qin, K.: In-tandem multi-waveband particulate absorption and size observations yield substantial changes in radiative forcing over industrial Central China, Atmos. Chem. Phys., 26, 3107–3123, https://doi.org/10.5194/acp-26-3107-2026, 2026a.

Guan, L., Cohen, J. B., Wang, S., Tiwari, P., Liu, Z., and Qin, K.: Improving aerosol absorption estimates via size-resolved constraints based on AERONET and in situ measurements, Geophys. Res. Lett., 53, e2025GL117418, https://doi.org/10.1029/2025GL117418, 2026b.

Haarig, M., Ansmann, A., Baars, H., Jimenez, C., Veselovskii, I., Engelmann, R., and Althausen, D.: Depolarization and lidar ratios at 355, 532, and 1064 nm and microphysical properties of aged tropospheric and stratospheric Canadian wildfire smoke, Atmos. Chem. Phys., 18, 11847–11861, https://doi.org/10.5194/acp-18-11847-2018, 2018.

Haarig, M., Ansmann, A., Engelmann, R., Baars, H., Toledano, C., Torres, B., Althausen, D., Radenz, M., and Wandinger, U.: First triple-wavelength lidar observations of depolarization and extinction-to-backscatter ratios of Saharan dust, Atmos. Chem. Phys., 22, 355–369, https://doi.org/10.5194/acp-22-355-2022, 2022.

Haarig, M., Engelmann, R., Baars, H., Gast, B., Althausen, D., and Ansmann, A.: Discussion of the spectral slope of the lidar ratio between 355 and 1064 nm from multiwavelength Raman lidar observations, *Atmos. Chem. Phys.*, **25**, 7741–7763, https://doi.org/10.5194/acp-25-7741-2025, 2025.

Hand, J. L. and Kreidenweis, S. M.: A new method for retrieving particle refractive index and effective density from aerosol size distribution data, Aerosol Sci. Technol., 36, 1012–1026, https://doi.org/10.1080/02786820290092276, 2002.

~~Hansen, J. E. and Travis, L. D.: Light scattering in planetary atmospheres, Space Sci. Rev., 16, 527–610, https://doi.org/10.1007/BF00168069, 1974.~~

Heim, M., Mullins, B. J., Umhauer, H., and Kasper, G.: Performance evaluation of three optical particle counters with an efficient "multimodal" calibration method, J. Aerosol Sci., 39, 1019–1031, https://doi.org/10.1016/j.jaerosci.2008.07.006, 2008.

Huang, Y., Kok, J. F., Saito, M., and Muñoz, O.: Single-scattering properties of ellipsoidal dust aerosols constrained by measured dust shape distributions, Atmos. Chem. Phys., 23, 2557–2577, https://doi.org/10.5194/acp-23-2557-2023, 2023.

Huber, P. J.: Robust estimation of a location parameter, Ann. Math. Stat., 35, 73–101, https://doi.org/10.1214/aoms/1177703732, 1964.

Kim, M.-H., Omar, A. H., Tackett, J. L., Vaughan, M. A., Winker, D. M., Trepte, C. R., Hu, Y., Liu, Z., Poole, L. R., Pitts, M. C., Kar, J., and Magill, B. J.: The CALIPSO version 4 automated aerosol classification and lidar ratio selection algorithm, Atmos. Meas. Tech., 11, 6107–6135, https://doi.org/10.5194/amt-11-6107-2018, 2018.

Koehler, K. A., Kreidenweis, S. M., DeMott, P. J., Petters, M. D., Prenni, A. J., and Carrico, C. M.: Hygroscopicity and cloud droplet activation of mineral dust aerosol, Geophys. Res. Lett., 36, L08805, https://doi.org/10.1029/2009GL037348, 2009.

Lack, D. A. and Langridge, J. M.: On the attribution of black and brown carbon light absorption using the Ångström exponent, Atmos. Chem. Phys., 13, 10535–10543, https://doi.org/10.5194/acp-13-10535-2013, 2013.

Li, H., Yang, T., Sun, Y., and Wang, Z.: A Physics-Constrained Deep-Learning Framework based on Long-Term Remote-Sensing Data for Retrieving Vertical Distribution of $PM_{2.5}$ Chemical Components, Atmos. Meas. Tech., 19, 2225–2244, https://doi.org/10.5194/amt-19-2225-2026, 2026.

Liu, X., Alves Gouveia, D., Henzing, B., Apituley, A., Hensen, A., van Dinther, D., Huang, R., and Dusek, U.: Aerosol optical properties within the atmospheric boundary layer predicted from ground-based observations compared to Raman lidar retrievals during RITA-2021, Atmos. Chem. Phys., 24, 9597–9614, https://doi.org/10.5194/acp-24-9597-2024, 2024.

Lucarini, V., Peiponen, K.-E., Saarinen, J. J., and Vartiainen, E. M.: Kramers–Kronig Relations in Optical Materials Research, Springer, Berlin, Heidelberg, https://doi.org/10.1007/b138913, 2005.

Mack, L. A., Levin, E. J. T., Kreidenweis, S. M., Obrist, D., Moosmüller, H., Lewis, K. A., Arnott, W. P., McMeeking, G. R., Sullivan, A. P., Wold, C. E., Hao, W.-M., Collett, J. L., and Malm, W. C.: Optical closure experiments for biomass smoke aerosols, Atmos. Chem. Phys., 10, 9017–9026, https://doi.org/10.5194/acp-10-9017-2010, 2010.

Masoom, A., Kazadzis, S., Modini, R. L., Gysel-Beer, M., Gröbner, J., Coen, M. C., Navas-Guzman, F., Kouremeti, N., Brem, B. T., Nowak, N. K., Martucci, G., Hervo, M., and Erb, S.: Long range transport of Canadian Wildfire smoke to Europe in Fall 2023: aerosol properties and spectral features of smoke particles, EGUsphere [preprint], https://doi.org/10.5194/egusphere-2025-2755, 2025.

Müller, D., Ansmann, A., Mattis, I., Tesche, M., Wandinger, U., Althausen, D., and Pisani, G.: Aerosol-type-dependent lidar ratios observed with Raman lidar, J. Geophys. Res.-Atmos., 112, D16202, https://doi.org/10.1029/2006JD008292, 2007.

Müller, D., Böckmann, C., Kolgotin, A., Schneidenbach, L., Chemyakin, E., Rosemann, J., Znak, P., and Romanov, A.: Microphysical particle properties derived from inversion algorithms developed in the framework of EARLINET, *Atmos. Meas. Tech.*, **9**, 5007–5035, https://doi.org/10.5194/amt-9-5007-2016, 2016.

Myhre, G., Samset, B. H., Schulz, M., Balkanski, Y., Bauer, S., Berntsen, T. K., Bian, H., Bellouin, N., Chin, M., Diehl, T., Easter, R. C., Feichter, J., Ghan, S. J., Hauglustaine, D., Iversen, T., Kinne, S., Kirkevåg, A., Lamarque, J.-F., Lin, G., Liu, X., Lund, M. T., Luo, G., Ma, X., van Noije, T., Penner, J. E., Rasch, P. J., Ruiz, A., Seland, Ø., Skeie, R. B., Stier, P., Takemura, T., Tsigaridis, K., Wang, P., Wang, Z., Xu, L., Yu, H., Yu, F., Yoon, J.-H., Zhang, K., Zhang, H., and Zhou, C.: Radiative forcing of the direct aerosol effect from AeroCom phase II simulations, Atmos. Chem. Phys., 13, 1853–1877, https://doi.org/10.5194/acp-13-1853-2013, 2013.

Ohta, K. and Ishida, H.: Comparison among several numerical integration methods for Kramers–Kronig transformation, Appl. Spectrosc., 42, 952–957, https://doi.org/10.1366/0003702884430380, 1988.

Ohneiser, K., Ansmann, A., Kaifler, B., Chudnovsky, A., Barja, B., Knopf, D. A., Kaifler, N., Baars, H., Seifert, P., Villanueva, D., Jimenez, C., Radenz, M., Engelmann, R., Veselovskii, I., and Zamorano, F.: Australian wildfire smoke in the stratosphere: the decay phase in 2020/2021 and impact on ozone depletion, Atmos. Chem. Phys., 22, 7417–7442, https://doi.org/10.5194/acp-22-7417-2022, 2022.

Omar, A. H., Winker, D. M., Vaughan, M. A., Hu, Y., Trepte, C. R., Ferrare, R. A., Lee, K.-P., Hostetler, C. A., Kittaka, C., Rogers, R. R., Kuehn, R. E., and Liu, Z.: The CALIPSO automated aerosol classification and lidar ratio selection algorithm, J. Atmos. Oceanic Technol., 26, 1994–2014, https://doi.org/10.1175/2009JTECHA1231.1, 2009.

Petters, M. D., and Kreidenweis, S. M.: A single parameter representation of hygroscopic growth and cloud condensation nucleus activity, Atmos. Chem. Phys., 7, 1961–1971, https://doi.org/10.5194/acp-7-1961-2007, 2007.

Pringle, K. J., Tost, H., Message, S., Steil, B., Giannadaki, D., Nenes, A., Fountoukis, C., Stier, P., Vignati, E., and Lelieveld, J.: Description and evaluation of GMXe: a new aerosol submodel for global simulations (v1), Geosci. Model Dev., 3, 391–412, https://doi.org/10.5194/gmd-3-391-2010, 2010.

Radney, J. G. and Zangmeister, C. D.: Comparing aerosol refractive indices retrieved from full distribution and size- and mass-selected measurements, J. Quant. Spectrosc. Radiat. Transfer, 220, 52–66, https://doi.org/10.1016/j.jqsrt.2018.08.021, 2018.

Sandradewi, J., Prévôt, A. S. H., Szidat, S., Perron, N., Alfarra, M. R., Lanz, V. A., Weingartner, E., and Baltensperger, U.: Using aerosol light absorption measurements for the quantitative determination of wood burning and traffic emission contributions to particulate matter, Environ. Sci. Technol., 42, 3316–3323, https://doi.org/10.1021/es702253m, 2008.

Schlosser, J. S., Dmitrovic, S., Bennett, R., Cairns, B., Chen, G., Diskin, G. S., Ferrare, R. A., Hair, J. W., Jones, M. A., Reid, J. S., Shingler, T. J., Shook, M. A., Sorooshian, A., Thornhill, K. L., Ziemba, L. D., and Stamnes, S.: Closing the gap: an algorithmic approach to reconciling in situ and remotely sensed aerosol properties, Atmos. Meas. Tech., 18, 7187–7220, https://doi.org/10.5194/amt-18-7187-2025, 2025.

Shin, S.-K., Tesche, M., Kim, K., Kezoudi, M., Tatarov, B., Müller, D., and Noh, Y.: On the spectral depolarisation and lidar ratio of mineral dust provided in the AERONET version 3 inversion product, Atmos. Chem. Phys., 18, 12735–12746, https://doi.org/10.5194/acp-18-12735-2018, 2018.

Titos, G., Burgos, M. A., Zieger, P., Alados-Arboledas, L., Baltensperger, U., Jefferson, A., Sherman, J., Weingartner, E., Henzing, B., Luoma, K., O'Dowd, C., Wiedensohler, A., and Andrews, E.: A global study of hygroscopicity-driven light-scattering enhancement in the context of other in situ aerosol optical properties, Atmos. Chem. Phys., 21, 13031–13050, https://doi.org/10.5194/acp-21-13031-2021, 2021.

Titos, G., Cazorla, A., Zieger, P., Andrews, E., Lyamani, H., Granados-Muñoz, M. J., Olmo, F. J., and Alados-Arboledas, L.: Effect of hygroscopic growth on the aerosol light-scattering coefficient: A review of measurements, techniques and error sources, Atmos. Environ., 141, 494–507, https://doi.org/10.1016/j.atmosenv.2016.07.021, 2016.

Turšič, J., Podkrajšek, B., Grgić, I., Ctyroky, P., Berner, A., Dusek, U., and Hitzenberger, R.: Chemical composition and hygroscopic properties of size-segregated aerosol particles collected at the Adriatic coast of Slovenia, Chemosphere, 63, 1193–1202, https://doi.org/10.1016/j.chemosphere.2005.08.040, 2006.

van Diedenhoven, B., Hasekamp, O. P., Cairns, B., Schuster, G. L., Stamnes, S., Shook, M., and Ziemba, L.: Remote sensing of aerosol water fraction, dry size distribution and soluble fraction using multi-angle, multi-spectral polarimetry, Atmos. Meas. Tech., 15, 7411–7434, https://doi.org/10.5194/amt-15-7411-2022, 2022.

Virkkula, A., Chi, X., Ding, A., Shen, Y., Nie, W., Qi, X., Zheng, L., Huang, X., Xie, Y., Wang, J., Petäjä, T., and Kulmala, M.: On the interpretation of the loading correction of the aethalometer, Atmos. Meas. Tech., 8, 4415–4427, https://doi.org/10.5194/amt-8-4415-2015, 2015.

Vratolis, S., Fetfatzis, P., Argyrouli, A., Papayannis, A., Müller, D., Veselovskii, I., Bougiatioti, A., Nenes, A., Remoundaki, E., Diapouli, E., Manousakas, M., Mylonaki, M., and Eleftheriadis, K.: A new method to retrieve the real part of the equivalent refractive index of atmospheric aerosols, J. Aerosol Sci., 117, 54–62, https://doi.org/10.1016/j.jaerosci.2017.12.013, 2018.

Wang, A., Yin, Z., Yi, Y., Dong, X., Lu, T., Müller, D., and Wang, X.: Multi-channel aerosol Raman polarization Lidar for 3α + 3β + 3δ and meteorological parameters profiling, Opt. Laser Technol., 203, 115893, https://doi.org/10.1016/j.optlastec.2026.115893, 2026.

Wagner, R., Testa, B., Höpfner, M., Kiselev, A., Möhler, O., Saathoff, H., Ungermann, J., and Leisner, T.: High-resolution optical constants of crystalline ammonium nitrate for infrared remote sensing of the Asian Tropopause Aerosol Layer, Atmos. Meas. Tech., 14, 1977–1991, https://doi.org/10.5194/amt-14-1977-2021, 2021.

Walser, A., Sauer, D., Spanu, A., Gasteiger, J., and Weinzierl, B.: On the parametrization of optical particle counter response including instrument-induced broadening of size spectra and a self-consistent evaluation of calibration measurements, Atmos. Meas. Tech., 10, 4341–4361, https://doi.org/10.5194/amt-10-4341-2017, 2017.

Wang, L., Yin, Z., Lu, T., Yi, Y., Dong, X., Dai, Y., Bu, Z., Chen, Y., and Wang, X.: 1064 nm rotational Raman polarization lidar for profiling aerosol and cloud characteristics, Opt. Express, 32, 14963–14977, https://doi.org/10.1364/OE.518259, 2024.

Wang, L., Bervida Mačak, M., Stanič, S., Bergant, K., Gregorič, A., Drinovec, L., Močnik, G., Yin, Z., Yi, Y., Müller, D., and Wang, X.: Investigation of aerosol types and vertical distributions using polarization Raman lidar over Vipava Valley, Remote Sens., 14, 3482, https://doi.org/10.3390/rs14143482, 2022.

Wang, L., Stanič, S., Bergant, K., Eichinger, W., Močnik, G., Drinovec, L., Vaupotič, J., Miler, M., Gosar, M., and Gregorič, A.: Retrieval of vertical mass concentration distributions—vipava valley case study, Remote Sens., 11, 106, https://doi.org/10.3390/rs11020106, 2019.

Wiedensohler, A., Birmili, W., Nowak, A., Sonntag, A., Weinhold, K., Merkel, M., Wehner, B., Tuch, T., Pfeifer, S., Fiebig, M., Fjäraa, A. M., Asmi, E., Sellegri, K., Depuy, R., Venzac, H., Villani, P., Laj, P., Aalto, P., Ogren, J. A., Swietlicki, E., Williams, P., Roldin, P., Quincey, P., Hüglin, C., Fierz-Schmidhauser, R., Gysel, M., Weingartner, E., Riccobono, F., Santos, S., Grüning, C., Faloon, K., Beddows, D., Harrison, R. M., Monahan, C., Jennings, S. G., O'Dowd, C. D., Marinoni, A., Horn, H.-G., Keck, L., Jiang, J., Scheckman, J., McMurry, P. H., Deng, Z., Zhao, C. S., Moerman, M., Henzing, B., de Leeuw, G., Löschau, G., and Bastian, S.: Mobility particle size spectrometers: harmonization of technical standards and data structure to facilitate high quality long-term observations of atmospheric particle number size distributions, Atmos. Meas. Tech., 5, 657–685, https://doi.org/10.5194/amt-5-657-2012, 2012.

Yao, C., Wang, L., and Huang, A.: Data and code for: A decoupled in situ framework for multi-wavelength aerosol optical properties: application for lidar retrievals, Zenodo [data set and code], https://doi.org/10.5281/zenodo.20606543, 2026.

Yus-Díez, J., Bernardoni, V., Močnik, G., Alastuey, A., Ciniglia, D., Ivančič, M., Querol, X., Perez, N., Reche, C., Rigler, M., Vecchi, R., Valentini, S., and Pandolfi, M.: Determination of the multiple-scattering correction factor and its cross-sensitivity to scattering and wavelength dependence for different AE33 aethalometer filter tapes: a multi-instrumental approach, Atmos. Meas. Tech., 14, 6335–6355, https://doi.org/10.5194/amt-14-6335-2021, 2021.

Yus-Díez, J., Drinovec, L., Alados-Arboledas, L., Titos, G., Bazo, E., Casans, A., Patrón, D., Querol, X., Gonzalez-Romero, A., Perez García-Pando, C., and Močnik, G.: Characterization of filter photometer artifacts in soot and dust measurements –

laboratory and ambient experiments using a traceably calibrated aerosol absorption reference, Atmos. Meas. Tech., 18, 3073–3093, https://doi.org/10.5194/amt-18-3073-2025, 2025.

Zhao, G., Zhao, W., and Zhao, C.: Method to measure the size-resolved real part of aerosol refractive index using differential mobility analyzer in tandem with single-particle soot photometer, Atmos. Meas. Tech., 12, 3541–3550, https://doi.org/10.5194/amt-12-3541-2019, 2019.

Zieger, P., Fierz-Schmidhauser, R., Weingartner, E., and Baltensperger, U.: Effects of relative humidity on aerosol light scattering: results from different European sites, Atmos. Chem. Phys., 13, 10609–10631, https://doi.org/10.5194/acp-13-10609-2013, 2013.

Zotter, P., Herich, H., Gysel, M., El-Haddad, I., Zhang, Y., Močnik, G., Hüglin, C., Baltensperger, U., Szidat, S., and Prévôt, A. S. H.: Evaluation of the absorption Åångström exponents for traffic and wood burning in the aethalometer-based source apportionment using radiocarbon measurements of ambient aerosol, Atmos. Chem. Phys., 17, 4229–4249, https://doi.org/10.5194/acp-17-4229-2017, 2017.